

Higgs couplings in SMEFT via Zh production at the HL-LHC

Subhaditya Bhattacharya,^a Sanjoy Biswas,^b Abhik Sarkar^a

^a*Department of Physics, Indian Institute of Technology Guwahati, Assam 781039, India*

^b*Department of Physics, Ramakrishna Mission Vivekananda Educational and Research Institute, Belur Math, Howrah 711202, India*

E-mail: subhab@iitg.ac.in, sanjoy.phy@gm.rkmvu.ac.in,
sarkar.abhik@iitg.ac.in

ABSTRACT: We study the Higgs couplings involved in the Zh associated production mode at the Large Hadron Collider (LHC) in presence of Higgs-gauge boson coupling modifiers via κ framework, and dimension 6 Standard Model Effective Theory (SMEFT) operators. The analysis is performed mainly in context of the HL-LHC (with $\sqrt{s}=14$ TeV and luminosity 3000 fb^{-1}) setup using cut based as well as machine learning techniques. The analysis shows significant betterment in the signal significance by using the machine learning technique. We also do a χ^2 analysis, which reveals an appreciable change in the sensitivity of the coupling modifiers due to the presence of effective operators, in particular due to the $qqZh$ Higgs-current interactions. The dipole operators concerning the same vertex, combine quarks of different chiralities and does not interfere with the SM diagrams, hence contributing only at $\mathcal{O}(\Lambda^{-4})$. In order to observe better sensitivity for this class of operators, we need to move to higher center-of-mass energy, where the effects of both Higgs-current and dipole 4-point interactions are more prominent.

KEYWORDS: Higgs Production, Higgs Properties, SMEFT.

Contents

1	Introduction	1
2	EFT framework	3
2.1	SMEFT operators relevant to Zh production	4
2.2	Parametrization of production cross sections	5
2.3	Comparison with other Higgs production modes	9
3	Constraints on the hZZ coupling from current data	10
3.1	Constraints on the effective coupling coefficients	11
4	Collider analysis: current and future runs	13
4.1	Cut based analysis	14
4.2	BDT based analysis	17
4.3	Two parameter χ^2 analysis	19
4.4	Other future pp colliders	21
5	Summary and conclusion	23
A	Constraints on operators	24
B	Details of BDT analysis	25
C	Differential distributions	27
D	Z branching correction	27
E	The effect of custodial symmetry	28

1 Introduction

The Higgs boson discovery at the LHC provided the first conclusive portrait of the Electroweak Symmetry Breaking (EWSB) mechanism [1] and mass generation of the SM particles. Over a decade since the Higgs discovery, we have been able to probe many of its properties, some of which are precise and closely mimic that of a SM-like isodoublet (H), some are not, allowing for New Physics (NP) studies via Higgs sector. One standard way of parametrizing the Higgs couplings beyond the SM is to use the κ framework [2], where any deviation from the SM is taken into consideration by variation of the κ parameter, where $\kappa = 1$ depicts SM. For example, concerning the hZZ coupling, the corresponding $\kappa_Z = \frac{g_{hZZ}}{g_{hZZ}^{SM}}$. Most of the Higgs studies at the LHC uses such parametrisation and so do

we. However, one needs to be vigilant about the possible sources of NP that generates such contributions and need to be consistent with null observation of NP searches while scanning the possible values that κ can acquire¹.

Over the last two runs, LHC experiments, ATLAS [3] and CMS [4] have almost pinned down the Higgs couplings to less than 10% uncertainty, however, the High Luminosity (HL) run will prove to be significant for establishing a clearer picture of Higgs characteristics. The Higgs couplings associated with gauge bosons has been studied extensively in the existing literature from various point of views. They include bounds on the anomalous couplings [5–9], Higgs CP properties [10–14], etc. The procedure involves dedicated signal observables as well as in the effective theory (EFT) framework [15–29] in variety of production and decay channels in context of the current and future colliders.

In this analysis, we study the NP effects in hZZ and qqZ couplings as well as the fully NP induced $qqZh$ coupling in the Zh associated production mode at the High Luminosity (HL) LHC frontier. We adhere to the κ framework to depict NP contribution coming to hZZ coupling, whereas the NP contributions to qqZ and $qqZh$ are studied within the realm of the Standard Model Effective Field Theory (SMEFT) [30]. SMEFT framework is arguably the best motivated scenario for searching NP in a model independent way, either via deviations in the signal pattern or excess in the cross-section predicted from the SM, given the absence of a specific hint for NP in current scenarios. We would also like to note here, that while the contributions to $\kappa_Z \neq 1$ may very well appear from the SMEFT operators, however, there are restrictions like Z mass corrections, which may constrain such contributions. Therefore, parametrising the hZZ coupling via κ_Z makes us explore possibilities even beyond SMEFT. In short, by using both κ framework and SMEFT, we are basically taking the leading contributions to the relevant couplings that affect the chosen process.

Out of the different channels of Higgs production, the Vh ($V = W, Z$) production cross-section turn out to be more sensitive to the variation of effective operators concerned in the modification of the aforementioned couplings. In this analysis, we study the Zh channel. There have been a number of analysis concerning the Wh/Zh production modes [16–22]. However, the effect of dipole contact operators in context of the $qqZ/qqZh$ couplings have been neglected. The effect of dipole operators have been studied in [31], but concerning the Wh mode only. We show that the presence of both Higgs-current as well as dipole contact operators appreciably alter the existing bounds on the concerned couplings at the present and projected LHC sensitivities.

The organization of the paper is as follows: we discuss SMEFT operators relevant for our analysis and their sensitivities in section 2, constraints on the coupling modifiers as well as SMEFT coefficients from current data in section 3, detailed collider analysis in section 4 and concluding remarks in 5.

¹We will address this issue later in a specific context.

2 EFT framework

The couplings of our interest for this study are the $qqZ/qqZh$ and hZZ vertices which appear in both VBF as well as Zh production modes of the Higgs boson. The set of interaction terms involve those connecting to the gauge fields, field strength tensor (or the dual of it) along with the Higgs field and quark bilinear with all possible Lorentz structure, adhering to $U(1)_{\text{EM}}$ gauge symmetry after EWSB, as furnished below.

$$\mathcal{L}_{SM} = g_{uL}^{\text{SM}} Z_\mu \bar{u}_L \gamma^\mu u_L + g_{uR}^{\text{SM}} Z_\mu \bar{u}_R \gamma^\mu u_R + g_{dL}^{\text{SM}} Z_\mu \bar{d}_L \gamma^\mu d_L + g_{dR}^{\text{SM}} Z_\mu \bar{d}_R \gamma^\mu d_R; \quad (2.1)$$

$$\mathcal{L}_\kappa = \kappa_Z \frac{m_Z^2}{v} Z_\mu Z^\mu h; \quad (2.2)$$

$$\begin{aligned} \mathcal{L}_{NP} = & g_{ZZ} \frac{h}{v} Z^{\mu\nu} Z_{\mu\nu} + g_{Z\tilde{Z}} \frac{h}{v} Z^{\mu\nu} \tilde{Z}_{\mu\nu} + g_{Z\gamma} \frac{h}{v} A^{\mu\nu} Z_{\mu\nu} + g_{\tilde{Z}\gamma} \frac{h}{v} A^{\mu\nu} \tilde{Z}_{\mu\nu} \\ & + g_u^L Z_\mu \bar{u}_L \gamma^\mu u_L + g_u^R Z_\mu \bar{u}_R \gamma^\mu u_R + g_d^L Z_\mu \bar{d}_L \gamma^\mu d_L + g_d^R Z_\mu \bar{d}_R \gamma^\mu d_R \\ & + \delta_u^L \frac{h}{v} Z_\mu \bar{u}_L \gamma^\mu u_L + \delta_u^R \frac{h}{v} Z_\mu \bar{u}_R \gamma^\mu u_R + \delta_d^L \frac{h}{v} Z_\mu \bar{d}_L \gamma^\mu d_L + \delta_d^R \frac{h}{v} Z_\mu \bar{d}_R \gamma^\mu d_R \\ & + g_u \frac{1}{v} (\bar{u}_L \sigma^{\mu\nu} u_R + \bar{u}_R \sigma^{\mu\nu} u_L) Z_{\mu\nu} + g_d \frac{1}{v} (\bar{d}_L \sigma^{\mu\nu} d_R + \bar{d}_R \sigma^{\mu\nu} d_L) Z_{\mu\nu} \\ & + \delta_u \frac{h}{v^2} (\bar{u}_L \sigma^{\mu\nu} u_R + \bar{u}_R \sigma^{\mu\nu} u_L) Z_{\mu\nu} + \delta_d \frac{h}{v^2} (\bar{d}_L \sigma^{\mu\nu} d_R + \bar{d}_R \sigma^{\mu\nu} d_L) Z_{\mu\nu}. \end{aligned} \quad (2.3)$$

Note here in writing Eq. (2.1–2.3), we have adhered to $H = \begin{pmatrix} 0 \\ \frac{v+h}{\sqrt{2}} \end{pmatrix}$ after EWSB. Here, κ_Z is the SM hZZ coupling modifier. The advantage of κ framework in addition to heavy integrable NP scenarios, it enables us to consider undetected light degrees of freedom without explicitly introducing a NP scale. In the above equations, the notations have their usual meanings, particularly note $Z_{\mu\nu} = \partial_\mu Z_\nu - \partial_\nu Z_\mu$, $\tilde{Z}_{\mu\nu} = \epsilon_{\mu\nu\alpha\beta} Z^{\alpha\beta}$ where Z_μ denotes the physical Z boson, $\epsilon_{\mu\nu\alpha\beta}$ is a completely antisymmetric tensor and $\sigma^{\mu\nu} = \frac{i}{2} [\gamma^\mu, \gamma^\nu]$.

In absence of a direct observational evidence of NP signal at current experiments, one of the best possible ways to gauge the effects of NP is through higher dimensional effective operators constructed out of the SM fields respecting the SM gauge symmetry. They are popularly referred as SMEFT operators. Note here that SMEFT operators also include the Higgs field as isodoublet under the SM gauge group, while there are efforts to keep it beyond, for example, in HEFT [32], but given the Higgs properties closely mimicking that of a SM doublet, we choose SMEFT framework to explore the limit of NP². These operators are suppressed by an appropriate power of a heavy NP mass scale (Λ) integrated out, depending on the mass-scale of the operator. Understandably the effects of such operators diminish with higher mass dimension of the operators, hence we will constrict ourselves to the lowest dimension operators that contribute to the Zh associated production, which appears in dimension 6³; operators of dimension 8 [39, 40] may also contribute, but we

²Operators with two Higgs doublets [33, 34], or a right handed neutrino [35–38] have also been found out.

³It is well known that the only SMEFT operator in dimension 5 is the Weinberg operator $\bar{N} N^c$; $N =$

have not considered them in our analysis. We will provide a detailed matching of Eq.2.3 with the standard SMEFT framework in Warsaw basis [41] later.

2.1 SMEFT operators relevant to Zh production

The SMEFT Lagrangian can be written as:

$$\mathcal{L} = \mathcal{L}_{SM} + \sum_{i, (n>4)} \frac{c_i}{\Lambda^{(n-4)}} \mathcal{O}_i^{(n)}, \quad (2.4)$$

Here, $\mathcal{O}_i^{(n)}$ represents operators of dimension n and c_i represents dimensionless couplings or Wilson's coefficients. Throughout this analysis, the effective scale is taken as $\Lambda = 1$ TeV, while the resulting bound or the sensitivity is obtained for the corresponding Wilson coefficient c_i . However, it is simple to understand that the limit on c_i can be rescaled easily for different choices of Λ , following, $\frac{c_i}{\Lambda^2} = \frac{c'_i}{\Lambda'^2}$. Although, the validity of effective limit depends on the choice of Λ , strictly speaking the center of mass (CoM) energy of the reaction should abide by $\sqrt{s} < \Lambda$. At hadron collider, it is difficult to ensure such a condition, we elaborate upon the possibility later.

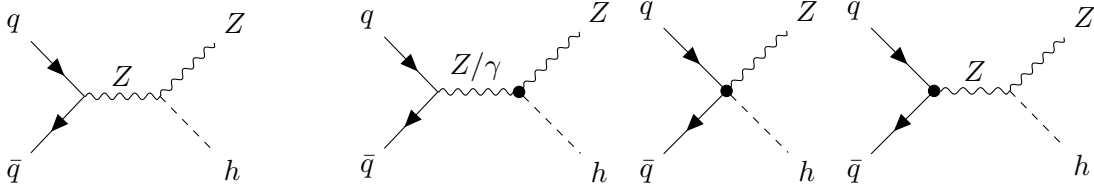


Figure 1: SM and EFT contributions to the Zh associated production mode at the LHC. Dotted vertices refer to the presence of EFT operators.

There is no unique basis for the choice of these operators and all the different bases are equivalent. We choose Warsaw basis for our representation. The SMEFT operators relevant to Zh associated production mode are tabulated in Table 1 and the corresponding Feynman diagrams are shown in Figure 1. The vertices with a blob represent effective operator contribution, which modifies hZZ , qqZ vertices and additional contributions are obtained via γZh and $qqZh$ vertices.

Before moving forward, it should be noted that operators are classified majorly into two categories, those generated at loop level (LG operators) or potential tree generated (PTG operators) for NPs those which are weakly coupled and decoupling [42]. The LG operators are suppressed additionally by a factor of $(4\pi)^2$ coming from the loops and hence their contributions are expected to be suppressed in comparison to the PTG operators if the underlying NP scale is the same. However, this additional suppression factor for the LG operators is not intrinsically incorporated in most SMEFT studies and in order to maintain uniformity of the nomenclature, we will however use the operator classification as in [41].

$H^\dagger \epsilon \ell$, which generates Majorana neutrino mass.

CP even hZZ vertex modifiers	Higgs-current operators
$\mathcal{O}_{H\Box} = (H^\dagger H)\Box(H^\dagger H)$	$\mathcal{O}_{Hq}^{(1)} = (H^\dagger i\overleftrightarrow{D}_\mu H)(\bar{q}_p\gamma^\mu q_r)$
$\mathcal{O}_{HDD} = (H^\dagger D_\mu H)(H^\dagger D^\mu H)$	$\mathcal{O}_{Hq}^{(3)} = (H^\dagger i\overleftrightarrow{D}_\mu^i H)(\bar{q}_p\tau^i\gamma^\mu q_r)$
$\mathcal{O}_{HW} = (H^\dagger H)W_{\mu\nu}^i W^{i\mu\nu}$	$\mathcal{O}_{Hu} = (H^\dagger i\overleftrightarrow{D}_\mu H)(\bar{u}_p\gamma^\mu u_r)$
$\mathcal{O}_{HB} = (H^\dagger H)B_{\mu\nu}B^{\mu\nu}$	$\mathcal{O}_{Hd} = (H^\dagger i\overleftrightarrow{D}_\mu H)(\bar{d}_p\gamma^\mu d_r)$
$\mathcal{O}_{HWB} = (H^\dagger \tau^i H)W_{\mu\nu}^i B^{\mu\nu}$	Dipole operators
CP odd hZZ vertex modifiers	$\mathcal{O}_{uW} = (\bar{q}_p\sigma^{\mu\nu}u_r)\tau^i\tilde{H}W_{\mu\nu}^i$
$\mathcal{O}_{H\tilde{W}} = (H^\dagger H)\tilde{W}_{\mu\nu}^i W^{i\mu\nu}$	$\mathcal{O}_{uB} = (\bar{q}_p\sigma^{\mu\nu}u_r)\tilde{H}B_{\mu\nu}$
$\mathcal{O}_{H\tilde{B}} = (H^\dagger H)\tilde{B}_{\mu\nu}B^{\mu\nu}$	$\mathcal{O}_{dW} = (\bar{q}_p\sigma^{\mu\nu}d_r)\tau^i\tilde{H}W_{\mu\nu}^i$
$\mathcal{O}_{H\tilde{W}B} = (H^\dagger \tau^i H)\tilde{W}_{\mu\nu}^i B^{\mu\nu}$	$\mathcal{O}_{dB} = (\bar{q}_p\sigma^{\mu\nu}d_r)\tilde{H}B_{\mu\nu}$

Table 1: Dimension 6 SMEFT operators: *Left:* hZZ vertex modifiers, *Right:* $qqZ/qqZh$ contact vertices (Higgs-current and dipole types), relevant to Vh associated production at the LHC. Here, p and r are quark family indices. For complex operators, the presence of respective hermitian conjugates is assumed. For relevance: $D_\mu = \partial_\mu + ig\frac{\tau^i}{2}W_\mu^i + ig'\frac{1}{2}B_\mu$, $W_{\mu\nu}^i = \partial_\mu W_\nu^i - \partial_\nu W_\mu^i + g\epsilon^{ijk}W_\mu^j W_\nu^k$, $B_{\mu\nu} = \partial_\mu B_\nu - \partial_\nu B_\mu$, $H^\dagger i\overleftrightarrow{D}_\mu H = iH^\dagger D_\mu H - i(D_\mu H)^\dagger H$, $H^\dagger i\overleftrightarrow{D}_\mu^i H = iH^\dagger \tau^i D_\mu H - i(D_\mu H)^\dagger \tau^i H$, $\tilde{V}_{\mu\nu} = \epsilon_{\mu\nu\rho\sigma}V^{\rho\sigma}$ ($V = W^i, B$).

A few observations related to the operators as mentioned in Table 1 are as follows: The operators $\mathcal{O}_{H\Box}$ and \mathcal{O}_{HDD} modify the Higgs gauge boson coupling by a multiplicative factor without introducing any new Lorentz structure, amounting to a renormalization of the Higgs field. As such the contribution can be absorbed in the coupling modifier. The operators \mathcal{O}_{HW} , \mathcal{O}_{HB} and \mathcal{O}_{HWB} contribute in the modification of the hZZ vertex. These amounts to the CP conserving anomalous Higgs gauge boson coupling. The operators $\mathcal{O}_{H\tilde{W}}$, $\mathcal{O}_{H\tilde{B}}$ and $\mathcal{O}_{H\tilde{W}B}$ contribute in the modification of the hZZ vertex. These amounts to the CP violating anomalous Higgs gauge boson coupling. The operators $\mathcal{O}_{Hq}^{(1)}$, $\mathcal{O}_{Hq}^{(3)}$, \mathcal{O}_{Hu} and \mathcal{O}_{Hd} contribute to the 4-point interaction $qqZh$. These operators also contribute to qqZ vertex. These operators are referred to as Higgs-current operators since their form is analogous to current, $j^\mu = \bar{\psi}\gamma^\mu\psi$. The operators \mathcal{O}_{uW} , \mathcal{O}_{uB} , \mathcal{O}_{dW} and \mathcal{O}_{dB} contribute to the 4-point interaction $qqZh$. These operators also contribute to qqZ vertex. These operators contribute to the dipole moments of quarks and hence can be referred to as dipole operators. A complete matching between the coefficients of \mathcal{L}_{NP} in Eq.2.1 and the SMEFT coefficients as in Table 1 are shown in Table 2.

2.2 Parametrization of production cross sections

When SMEFT effects are included, the cross section consists of three types of terms viz. the pure SM contribution, the SM plus EFT interference ($\propto \Lambda^{-2}$ from dimension six operators) and the pure EFT contribution ($\propto \Lambda^{-4}$). Inclusion of dimension 8 operators would result in SM plus EFT interference contribution $\propto \Lambda^{-4}$ which is comparable to the pure EFT contribution from dimension 6 terms, however, we do not consider them in this analysis.

Coefficient	Warsaw equivalent
g_{ZZ}	$2 (c_w^2 c_{HW} + s_w^2 c_{HB} + s_w c_w c_{H\widetilde{W}B}) v^2 / \Lambda^2$
$g_{Z\gamma}$	$(2 s_w c_w^2 (c_{HW} - c_{HB}) + (s_w^2 - c_w^2) c_{H\widetilde{W}B}) v^2 / \Lambda^2$
$g_{Z\widetilde{Z}}$	$2 (c_w^2 c_{H\widetilde{W}} + s_w^2 c_{H\widetilde{B}} + s_w c_w c_{H\widetilde{W}B}) v^2 / \Lambda^2$
$g_{\widetilde{Z}\gamma}$	$(2 s_w c_w^2 (c_{H\widetilde{W}} - c_{H\widetilde{B}}) + (s_w^2 - c_w^2) c_{H\widetilde{W}B}) v^2 / \Lambda^2$
g_u^L	$-\left(c_{Hq}^{(1)} + c_{Hq}^{(3)}\right) ev^2 / (2\Lambda^2 s_w c_w)$
g_d^L	$-\left(c_{Hq}^{(1)} - c_{Hq}^{(3)}\right) ev^2 / (2\Lambda^2 s_w c_w)$
g_u^R	$-c_{Hu} ev^2 / (2\Lambda^2 s_w c_w)$
g_d^R	$-c_{Hd} ev^2 / (2\Lambda^2 s_w c_w)$
δ_u^L	$-\left(c_{Hq}^{(1)} + c_{Hq}^{(3)}\right) ev^2 / (\Lambda^2 s_w c_w)$
δ_d^L	$-\left(c_{Hq}^{(1)} - c_{Hq}^{(3)}\right) ev^2 / (\Lambda^2 s_w c_w)$
δ_u^R	$-c_{Hu} ev^2 / (\Lambda^2 s_w c_w)$
δ_d^R	$-c_{Hd} ev^2 / (\Lambda^2 s_w c_w)$
g_u	$(s_w c_{uB} - c_w c_{uW}) ev^2 / \sqrt{2} \Lambda^2$
g_d	$(s_w c_{dB} + c_w c_{dW}) ev^2 / \sqrt{2} \Lambda^2$
δ_u	$\sqrt{2} (s_w c_{uB} - c_w c_{uW}) ev^2 / \Lambda^2$
δ_d	$\sqrt{2} (s_w c_{dB} + c_w c_{dW}) ev^2 / \Lambda^2$

Table 2: Matching between coefficients in equation (2.3) and the SMEFT coefficients. s_w and c_w are the sine and cosine of the Weinberg angle.

The production cross section in presence of SMEFT operators takes the form:

$$\sigma = \sigma^{(SM)} + \sum_{i=1}^{n_L} c_i \sigma_i^{(L)} + \sum_{i \leq j}^{n_Q} c_i c_j \sigma_{ij}^{(Q)}, \quad (2.5)$$

where, n_L and n_Q refers to the number of linear and quadratic SMEFT contributions. The effective scales Λ^{-2} and Λ^{-4} are absorbed in the cross sections $\sigma_i^{(L)}$ and $\sigma_{ij}^{(Q)}$ respectively. In presence of coupling modifiers κ , the cross section in equation (2.5) takes the form as below,

$$\begin{aligned} \sigma &= \kappa^2 \sigma^{(SM)} + \sum_{i=1}^{n_L} (\alpha_i^{(L)} \kappa + \beta_i^{(L)} \kappa^2) c_i \sigma_i^{(L)} + \sum_{i \leq j}^{n_Q} (1 + \alpha_{ij}^{(Q)} \kappa + \beta_{ij}^{(Q)} \kappa^2) c_i c_j \sigma_{ij}^{(Q)}, \\ \mu &= \kappa^2 + \sum_{i=1}^{n_L} (\alpha_i^{(L)} \kappa + \beta_i^{(L)} \kappa^2) c_i \mu_i^{(L)} + \sum_{i \leq j}^{n_Q} (1 + \alpha_{ij}^{(Q)} \kappa + \beta_{ij}^{(Q)} \kappa^2) c_i c_j \mu_{ij}^{(Q)}, \end{aligned} \quad (2.6)$$

where, μ is the signal strength, i.e. $\mu = \sigma / \sigma_{SM}$. Differential cross sections can be parametrized in a similar manner. At the hadron collider, an analytical form of the cross section is difficult to write due to the uncertainty of the incoming momenta of the partons. However, we can numerically fit the production cross section as a function of the parameters and this turns out to be equally useful for gauging the effects of NP. In the following, we fit the operator coefficients following (2.6) at 14 TeV LHC for the Zh associated production

process considering one operator at a time. The variation of the total production cross section are shown in Figure 2 (for CP even hZZ modifiers and Higgs-current operators) and 3 (for CP odd hZZ modifiers and dipole operators). The ratio of the total production cross section for moving from 13 TeV to 14 TeV are also shown. We adopt the following methodology, the effective Lagrangian is implemented in **FeynRules** [43] to generate the **UFO** model [44] file. The model file is validated with standard UFOs like **SMEFTsim** [45] and **SMEFTatNLO** [46]. This model file is then fed into the event generator **MG5_aMC** [47] to obtain the above cross sections at the leading order (LO). The cross sections are generated at production level without decaying Z or h to any specific decay mode without any kinematic cuts. The PDF set and flavor scheme choice are NN23L01 PDF set and $U(2)_q \times U(2)_u \times U(2)_d$, respectively. The NP scale is chosen as $\Lambda = 1$ TeV. A few key points observed are as follows: The Higgs-current operators have significant linear as well as quadratic contributions indicating large pure EFT contribution. The enhancement of the EFT terms result from the absence of propagator suppression in the production process. The dipole operators have no linear contribution. This is because they bind fermions with different chiralities and hence do not interfere with the SM process. Due to the absence of linear dependence, they cause variation in the cross section only in the positive direction. All the operators except $\mathcal{O}_{Hq}^{(3)}$ shows near symmetric behaviour along the positive and negative side. The operator $\mathcal{O}_{Hq}^{(3)}$ dips around $c_{Hq}^{(3)} = -0.2$ and then continues to rise as we go further in the negative direction. This is due to strong linear as well as quadratic dependence and the trade off between them happens away from $c_{Hq}^{(3)} = 0$ towards the negative axis. When moving from 13 TeV to 14 TeV LHC, the contact operators i.e. operators associated with $qqZ/qqZh$ vertices, significantly boost the production cross sections. The other operators are less sensitive.

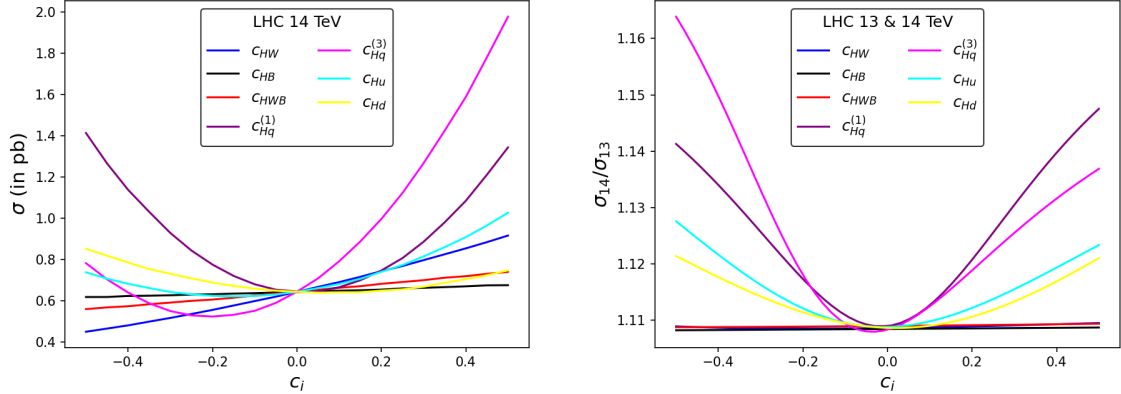


Figure 2: *Left:* Variation of Zh associated production cross section with variation in CP even hZZ modifiers and Higgs-current effective operator coefficients at the 14 TeV LHC. *Right:* Variation in the ratio of production cross section of the 14 TeV LHC to the 13 TeV LHC with variation in the effective operator coefficients. See figure inset for the colour codes.

For our analysis, we consider the two operators $\mathcal{O}_{Hq}^{(3)}$ and \mathcal{O}_{uW} as a representative of the Higgs-current and dipole class respectively. It should be noted that the choice is

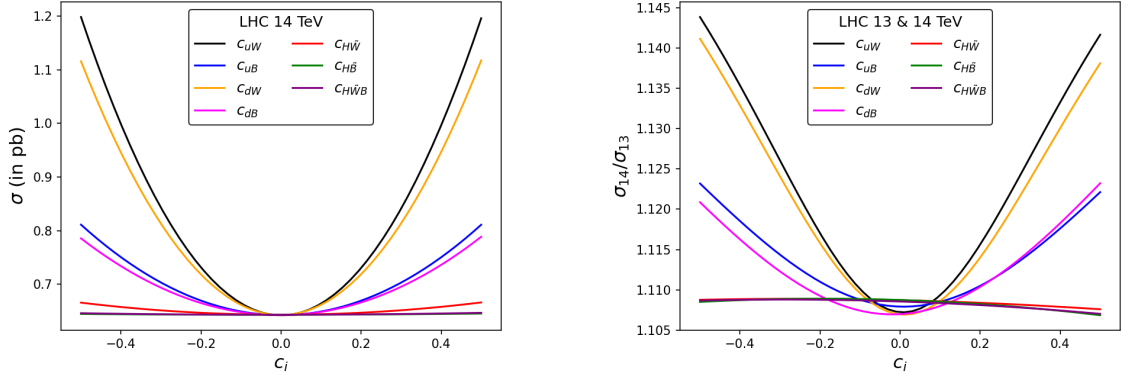


Figure 3: *Left:* Variation of Zh associated production cross section with change in CP odd hZZ modifiers and dipole effective operator coefficients at the 14 TeV LHC. *Right:* Variation in the ratio of production cross section of the 14 TeV LHC to the 13 TeV LHC with change in effective operator coefficients. See figure inset for the colour codes.

based on their sensitivity to the production cross section, however other operators from the respective classes maybe more sensitive to particular observables or be less bounded from experiments. Our consideration is based on proof of concept and any other operator can be chosen in lieu of these. Along with the coupling modifier κ_Z (which approximately estimates the EFT effect to the hZZ vertex), this form our EFT parameter space: $\{\kappa_Z, c_{uW}, c_{Hq}^{(3)}\}$. The parametrized coefficients for signal strength associated with Zh production with these operators following Eqn. (2.6) are tabulated in Table 3. This parametrization gives an overview of the EFT effects on the inclusive cross section. Coefficients of linear terms in $1, \kappa_Z, c_{uW}$ and $c_{Hq}^{(3)}$ are not present in our parametrization as it is evident from Eq. (2.6) that the interference between SM and SMEFT vertices appear as coefficient of $\kappa_Z c_{Hq}^{(3)}$. Further, the coefficients of $\kappa_Z c_{uW}, \kappa_Z^2 c_{uW}, c_{uW} c_{Hq}^{(3)}, \kappa_Z c_{uW} c_{Hq}^{(3)}$ and $\kappa_Z^2 c_{uW} c_{Hq}^{(3)}$ vanish because of no interference between the SM and $\mathcal{O}_{Hq}^{(3)}$ operators with diagrams with \mathcal{O}_{uW} operator as the dipole operator mixes quarks of different chiralities ($\bar{q}_L \sigma_{\mu\nu} q_R / \bar{q}_R \sigma_{\mu\nu} q_L$) in contrary to the SM or Higgs-current operators which mixes quarks of same chirality ($\bar{q}_L \gamma_\mu q_L / \bar{q}_R \gamma_\mu q_R$).

We shall also note that the variation of the cross-section presented here with EFT operator coefficients, have been done without considering the constraints on these operators. We shall do it in the next section. We get the dominant physics contribution to the process under consideration and the resultant parametrisation, which remains intact with the modified range of the operator coefficients that will be used for scanning the parameter space.

It should be further noted that due to the presence of momentum dependence in EFT vertices or absence of propagators, effect of EFT operators are evident mostly at the tails of differential distribution. Hence, presence of EFT, if any, can be best interpreted from changes to the differential distributions. Figure 4 shows the ratio of the invariant mass

Coefficients	1×1	$1 \times c_{uW}$	$1 \times c_{Hq}^{(3)}$	$c_{uW} \times c_{uW}$	$c_{Hq}^{(3)} \times c_{Hq}^{(3)}$	$c_{uW} \times c_{Hq}^{(3)}$
1×1	—	—	—	3.0277	4.2429	—
$1 \times \kappa_Z$	—	—	1.7060	0.2106	0.3880	—
$\kappa_Z \times \kappa_Z$	1.0000	—	0.1439	0.2000	-0.0472	—

Table 3: The parametrized coefficients (μ_i, μ_{ij}) for operators $\mathcal{O}_{Hq}^{(3)}$, \mathcal{O}_{uW} and κ_Z contributing to Zh production at 14 TeV LHC, following equation (2.6).

distribution, $M_{Zh} = \sqrt{(p_Z + p_h)^2}$ for Zh production in the presence of EFT operators to the corresponding SM prediction at the 14 TeV LHC.

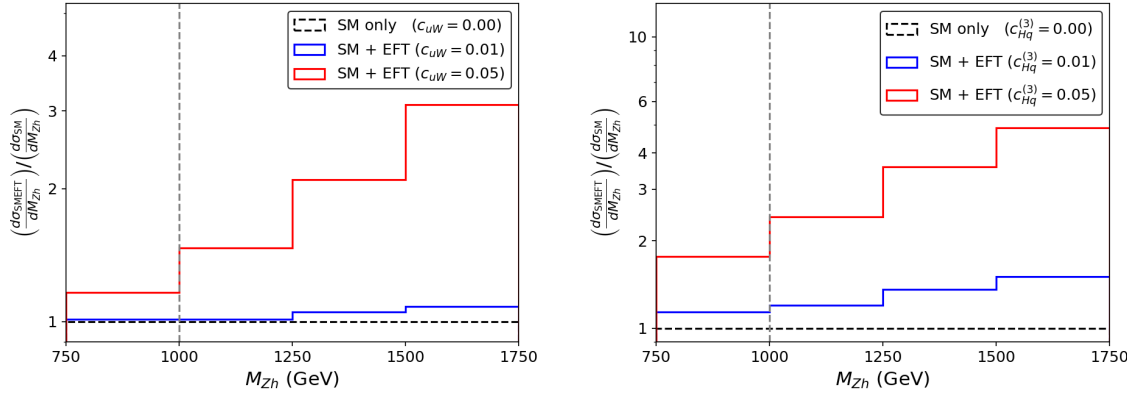


Figure 4: *Left:* Ratio of the invariant mass distribution, M_{Zh} for Zh production in presence of \mathcal{O}_{uW} operator to the corresponding SM prediction at the LHC 14 TeV. *Right:* Same for $\mathcal{O}_{Hq}^{(3)}$ operator. The grey vertical line refers to the EFT scale, $\Lambda = 1$ TeV.

2.3 Comparison with other Higgs production modes

The operators \mathcal{O}_{uW} and $\mathcal{O}_{Hq}^{(3)}$ are not unique to the Vh ($V = W, Z$) associated production mode. It appears in the vector boson fusion (VBF) and single top production in association with Higgs (thj) as well. The thj process has a comparatively smaller cross section and it is not ideal for the study of these operators, but the VBF mode has a larger cross section compared to Vh associated production mode, as considered here. These operators are also associated with the diboson production ($VV = WW, WZ, ZZ$) processes. However, the ratio of the signal production cross-section including EFT and that of the SM contribution is more sensitive to the changes in the Wilson coefficients in Vh mode compared to that of VBF and VV channels. This has been illustrated in Figure 5 for the operators $\mathcal{O}_{Hq}^{(3)}$ (left) and \mathcal{O}_{uW} (right)⁴. Also, for both VV and VBF modes, pure contact interaction diagrams are absent, so EFT contributions always come in presence of one or more propagators. Hence, for the study of $qqZ/qqZh$ vertices, Zh production is considered in our analysis.

⁴One should however note here that the sensitivity of a specific channel not only depends the signal cross-section, but also relies on the background contribution and the efficiency in extracting the signal.

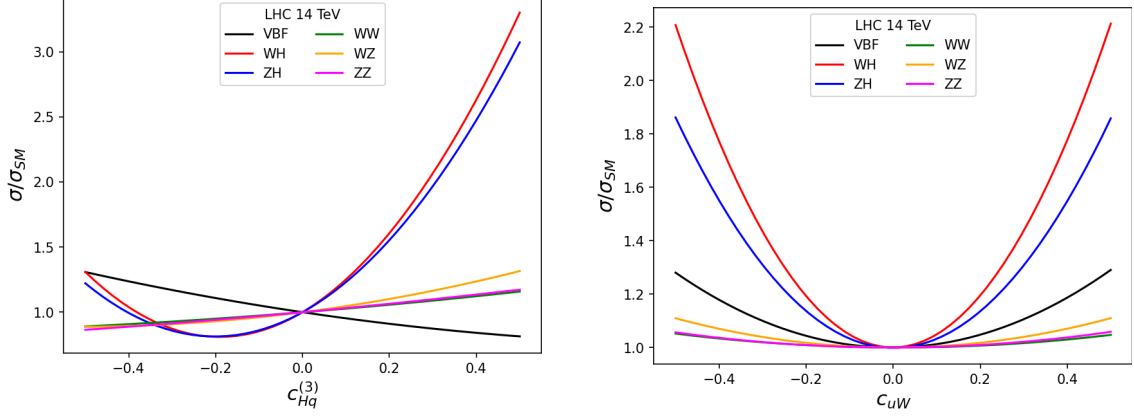


Figure 5: *Left:* Variation in the ratio of production cross section to the SM cross section in VBF, Vh and VV processes at the 14 TeV LHC with variation in effective coefficient $c_{Hq}^{(3)}$. *Right:* Same for c_{uW} .

3 Constraints on the hZZ coupling from current data

The κ framework is the most preferred way to incorporate uncertainties in the measurement of Higgs couplings. This has been adopted in most of the experimental results reported so far, and we will also follow the same here. The current uncorrelated bounds from ATLAS (139 fb^{-1}) and CMS (138 fb^{-1}) are based on Run II data and involves global fit over the main five production and decay channels. Since we intend to study Zh associated production with h subsequently decaying to bottom pair, the bottom Higgs coupling modifier, κ_B is also important for this analysis. Higgs decay to bottom pair has been studied intensely at the LHC across several channels and the bounds are given in terms of signal strength (μ), i.e. the ratio of the observed signal to the SM predicted value. In Table 5 we list out the uncorrelated bounds on the coupling modifiers as well as the signal strengths of the Higgs decay to bottom pair in the Zh production channel.

Measurable	Bound	Source
κ_Z	[0.97, 1.11]	CMS ($pp \rightarrow h$) [4]
	[0.94, 1.05]	ATLAS ($pp \rightarrow h$) [3]
κ_B	[0.85, 1.11]	CMS ($pp \rightarrow h$) [4]
	[0.79, 1.01]	ATLAS ($pp \rightarrow h$) [3]
μ_{hbb}^{Zh}	[0.59, 1.17]	CMS ($pp \rightarrow Zh, h \rightarrow b\bar{b}$) [48]
	[0.85, 1.33]	ATLAS ($pp \rightarrow Zh, h \rightarrow b\bar{b}$) [49]

Table 4: Constraints on κ_Z , κ_B and μ_{Hbb}^{Zh} (at 95% C.L.) from ATLAS and CMS experiments.

Considering the bounds on the signal strength, we can limit the coupling modifiers using the measured signal strengths as shown in Eqn. 3.1.

$$\mu_{hbb}^{Zh} = \frac{(\sigma^{Zh} \times (B.R.)_{hbb})}{(\sigma^{Zh} \times (B.R.)_{hbb})_{SM}} = \frac{\kappa_Z^2 \kappa_B^2}{0.1775 + 0.5809 \kappa_B^2 + 0.2416 \kappa_Z^2}. \quad (3.1)$$

In evaluating Eqn. 3.1, both the Higgs couplings with the bottom quark as well as with Z bosons have been modified keeping coupling with other fermions unchanged. κ_Z appears from the production cross-section, while κ_B appears from the decay branching fraction, pertaining to the fact that Higgs production and decay modes are those predicted in the SM, the NP effects only enters via rescaling of the Higgs coupling strength. The denominator comes from the modification of the Higgs decay width, which is easily adjusted within the observed total Higgs decay width at LHC for moderate values of κ parameters. We can see that for $\kappa_Z = \kappa_B = 1$, the signal strength turns one. We further invoke the custodial symmetry requirement $\kappa_W = \kappa_Z$. This assumption reduces the number of free parameters in the model and is consistent with the LHC bounds reported in [3, 4]. However, this assumption can be relaxed, and the impact of doing so in our analysis is discussed in Appendix E. The bounded region is shown in Figure 6. Additionally, superimposing the current correlated bound on the $\kappa_V - \kappa_F$ space from the combined Higgs measurement gives the status of the most accurate constraint from the current data. The uncertainties are less than 10% from the SM prediction.

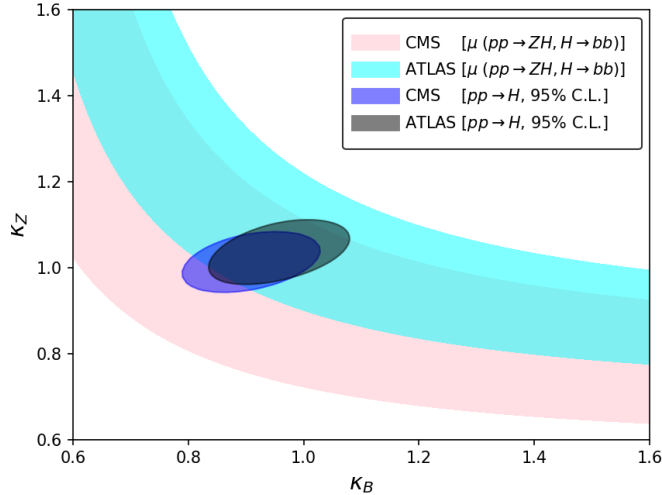


Figure 6: Constraints on coupling modifiers κ_Z and κ_B based on combined limit on $pp \rightarrow Zh$, $h \rightarrow b\bar{b}$ production signal strength (bands) [48, 49] as well as the combined experimental best fit from all Higgs production and decay processes (ellipses) [3, 4] at ATLAS and CMS experiments.

3.1 Constraints on the effective coupling coefficients

In context of the study of Higgs couplings in effective framework, several collaborations [50–54] has attempted to provide global bounds based on Higgs, Top and Diboson data from Tevatron, LHC and LEP. Similar fits have been done including B-Physics data with LHC top and bottom quark studies [55, 56]. Similarly, global fits have also been performed

based on Electroweak Precision data as well as Δ_{CKM} measurement [57]. Customarily, both ATLAS and CMS have done a number of studies on constraining the EFT operators across various channels using latest data. While ATLAS uses SMEFT, CMS uses HEL parametrization, we will consider bounds from ATLAS [49, 58–60] only. Also, there have been numerous studies concerning SMEFT, projecting constraints for future collider experiments [61–63]. We tabulate the constraints on the coefficients c_{uW} and $c_{Hq}^{(3)}$ from current data in Table 5 and 6. The constraints on other dipole and Higgs-current operators are listed in Appendix A.

Coefficient	Bound	C.L.	Flavor Scheme [Source]
c_{uW}	[-0.375, 0.375]	95%	$U(3)_q \times U(3)_u \times U(3)_d$ [64]
	[-0.290, 0.290]	95%	$U(2)_q \times U(2)_u \times U(2)_d$ [65]
	[-0.084, 0.029]	95%	$U(1)_Q \times U(1)_t$ [50]
	[-0.012, 0.048]	90%	$U(3)_q \times U(3)_u \times U(3)_d$ [56]
	[-0.079, 0.109]	95%	$U(1)_Q \times U(1)_t$ [54]
	[-0.120, 0.510]	95%	$U(1)_Q \times U(1)_t$ [51]

Table 5: Constraints on dipole operator coefficient c_{uW} from existing studies, see the references for details. q , u and d are the SM LH quark doublet, RH up and down-type quark singlets, respectively. Q and t refers to the third generation LH quark doublet and RH Top quark singlet, respectively.

Coefficient	Bound	C.L.	Flavor Scheme [Source]
$c_{Hq}^{(3)}$	[-0.432, 0.062]	95%	$U(2)_q \times U(2)_u \times U(3)_d$ [50]
	[-0.375, 0.344]	95%	$U(1)_Q \times U(1)_t$ [50]
	[-0.702, 0.104]	68%	$U(3)_q \times U(3)_u \times U(3)_d$ [57]
	[-0.080, 0.100]	95%	$U(3)_q \times U(3)_u \times U(3)_d$ [59]
	[-0.018, 0.026]	68%	$U(3)_q \times U(3)_u \times U(3)_d$ [49]
	[-0.150, 0.520]	95%	$U(3)_q \times U(3)_u \times U(3)_d$ [58]
	[-0.023, 0.053]	90%	$U(3)_q \times U(3)_u \times U(3)_d$ [56]
	[-0.017, 0.012]	95%	$U(2)_q \times U(2)_u \times U(3)_d$ [51]
	[-0.032, 0.048]	95%	$U(1)_Q \times U(1)_t$ [51]
	[-0.008, 0.016]	95%	$U(2)_q \times U(2)_u \times U(3)_d$ [53]

Table 6: Constraints on Higgs-current operator coefficient $c_{Hq}^{(3)}$ from existing studies, see the references for details.

A few comments and clarifications on the existing bounds: The bounds in Table 5 and 6 are individual bounds for the operator coefficients, where all other operator coefficient values are set to zero. The bounds for some of the studies in Table 5 and 6 are provided for (c/Λ^2) or (cv^2/Λ^2) . The values provided on the tables are normalized to $\Lambda = 1$ TeV. The flavor schemes associated with different analyses are tabulated as well in the tables. The bounds significantly change as per flavor assumptions. In this analysis, we will assume a $U(2)_q \times U(2)_u \times U(2)_d$, stating that the third generation is completely decoupled from the first two generations. This assumption is guided by the fact that the collisions at LHC

contributing to Zh production are evidently light quarks (b quark collisions are suppressed by PDFs). The bounds are from different analyses at difference confidence levels. For our analysis in succeeding sections, we consider the EFT benchmarks: $c_{uW} = 0.01, 0.05$ and $c_{Hq}^{(3)} = \pm 0.01, \pm 0.05$. Since, only the flavor scheme of [65] match with our flavor scheme, we only adhere to their bounds for c_{uW} . For $c_{Hq}^{(3)}$, none of the flavor scheme matches with our choice and we need not adhere to any of them. Still numerically, for c_{uW} , the benchmark 0.01 is consistent with all the bounds in Table 5, while the benchmark 0.05 is consistent with [51, 54, 64, 65] only. Similarly, for $c_{Hq}^{(3)}$, the benchmark 0.01 is consistent with all the bounds in Table 6, while -0.01 is not consistent with [53]. The benchmarks 0.05 and -0.05 are more wishful, and is incompatible with [49, 51, 53] and [49, 51, 53, 56], respectively, caveat to the flavor assumptions. The CP-violating gauge-Higgs operators listed in Table 1 are constrained by the fermion dipole moment observables, such as electron and neutron dipole moments, as they contribute at one loop to dipole operators. The current limits on the electron and neutron dipole moments are 1.1×10^{-29} and 3.0×10^{-26} (in units of e cm), respectively [66]. These operators are also constrained by the measurements of the triple gauge-interactions of the form $WW\gamma$ and WWZ at LEP and the CP asymmetry measured in the $B \rightarrow X_s \gamma$ decay. The CP asymmetry measured in $B \rightarrow X_s \gamma$ decay is $A_{B \rightarrow X_s \gamma} = 0.015(20)$. Bound on the imaginary part of dipole operator c_{uW} from neutron EDM [67] (assuming $U(2)_q \times U(2)_u \times U(2)_d$ flavor scheme) is shown below:

$$\Im(c_{uW}) < 0.000672 \quad (3.2)$$

The bound on other dipole operators are listed in Appendix A. The bounds are extremely stringent, hence difficult to probe at collider experiments. For our case, we restrict ourselves to the real dipole coefficients, hence evading these bounds. The bounds on light quark dipole operators from electron EDM appear at two loop involving a Yukawa interaction in the loop and hence are insignificant in comparison to other constraints [68].

4 Collider analysis: current and future runs

In this section, we will discuss the event generation and analysis in the context of the current and future HL LHC data. We have simulated $pp \rightarrow Zh \rightarrow (l^+ l^-)(b\bar{b})$ process at the LHC 13 TeV and 14 TeV center of mass energies. The PDF set used is NN23L01 [69] and the renormalization and factorization scales are set at the default dynamical scale choice of MadGraph. The signal and background informations will be detailed in Section 4.1. Before proceeding for a collider analysis in presence of the EFT operators, it is important to check validity of the effective approximation for the collider setup. The validity condition is $\sqrt{\hat{s}} < \Lambda$, where $\sqrt{\hat{s}}$ is the partonic centre of mass energy. However, ensuring this criteria is difficult in hadron colliders like LHC, where collisions between partons happen at variable centre of mass energies. One way to deal with this is to construct the invariant mass of the final state particles, M_{Zh} to guess the energy scale at which the partonic collisions take place. This is depicted in Figure 7, for the production process at a particular EFT benchmark point and we observe that almost all the events obey the effective validation

criteria, when $\Lambda = 1$ TeV. Now, the generated signal and background events are fed in **Pythia8** [70] for parton showering. The showered events are fed in **Fastjet3** [71] for jet clustering using the **anti- k_t** algorithm [72] with jet radius 0.5 and jet $p_T \geq 20$ GeV. Finally, the events are processed through **Delphes3**, using the card **delphes_card_cms**, to take into account finite detector resolution effects, as well as particle identification, reconstruction and jet tagging. The processed events are analyzed using **MadAnalysis5** [73].

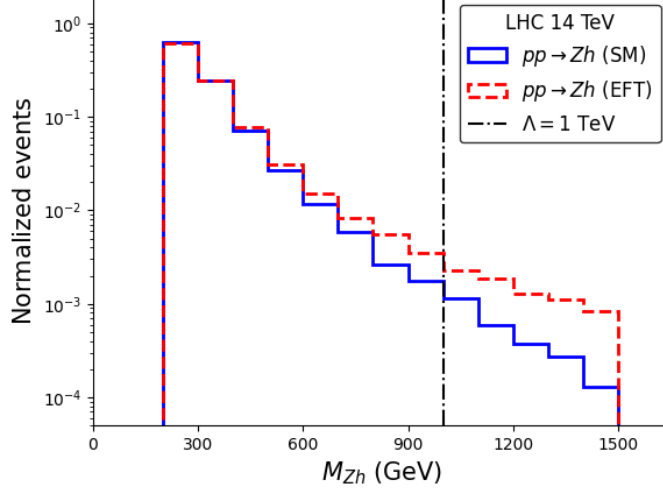


Figure 7: Invariant mass of Zh for the parton level processes in absence as well as presence of EFT operators at $\Lambda = 1$ TeV.. Here we consider the EFT benchmark point corresponding to $\{\kappa_Z, c_{uW}, c_{Hq}^{(3)}\} = \{1.00, 0.05, 0.05\}$.

4.1 Cut based analysis

We consider the signal to be $pp \rightarrow Z(l^+l^-)H(b\bar{b})$ i.e. a dilepton di-bjet signal. This signal is comparatively clean due to the presence of charged leptons with invariant mass of the dilepton system peaking around Z -mass. The possible SM backgrounds for this signal process are $pp \rightarrow t\bar{t}$, $pp \rightarrow ZZ$, $gg \rightarrow Zh$ and $pp \rightarrow Zb\bar{b}$. NLO corrections to both signal and background processes are taken into account by multiplying the production cross sections for each process by its NLO K factor, where $K = \sigma_{NLO}/\sigma_{LO}$. The LO and NLO cross sections are calculated using **MG5_aMC@NLO** at LHC 13 TeV and the K factors for different processes are: Zh : 1.288 (for $pp \rightarrow Zh$), 2.000 (for $gg \rightarrow Zh$), $Zb\bar{b}$: 1.230, $t\bar{t}$: 1.338 and ZZ : 1.461 [74–76].

We perform the analysis for two different setups viz. LHC 13 TeV 139 fb^{-1} (equivalent to Run II) and LHC 14 TeV 3000 fb^{-1} (future HL-LHC projection). We introduce some basic cuts common for all the analysis. These can be detailed as: $P_T^j > 20.0$ GeV, $P_T^l > 10.0$ GeV, $-5.0 < \eta_j < 5.0$, $-2.5 < \eta_l < 2.5$, $\Delta R_{jj} > 0.4$, $\Delta R_{lj} > 0.4$, $\Delta R_{ll} > 0.4$, where, subscripts j and l refer to jets and leptons respectively, and the kinematic variables have their usual definitions as in collider literature [77]. Apart from these, to ensure exclusive $l^+l^-b\bar{b}$ signal we select events with $N_b = 2$ and $N_l = 2$. The relevant distributions of kinematic variables and observables are plotted in Figure 8 for 13 TeV and 14 TeV LHC.

Choosing $N_j < 5$ for Zh considerably reduces the pure hadronic backgrounds at LHC. We further choose a wide M_{bb} cut around the Higgs mass to make sure that we retain most of the signal while eliminating the backgrounds. The presence of dileptons enables us to use some additional cuts. Owing to the better detectability of leptons, a narrow cut on M_{ll} around the Z mass significantly reduces the $t\bar{t}$ background. Finally due to the absence of invisible particles in the final state (a part from neutrinos possibly coming b -decay) rejecting events with large missing transverse energy, MET (MET > 30 GeV) removes backgrounds with neutrinos in final state like leptonic $t\bar{t}$ mode. The entire cut flow for SM Zh process (in absence of EFT contributions) is tabulated in Table 7.

	LHC 13 TeV 139 fb^{-1}				LHC 14 TeV 3000 fb^{-1}			
Cuts	S	B	S/B	z	S	B	S/B	z
Basic Cuts	569	1016890	0.0006	0.56	13327	25581580	0.0005	2.63
$N_j < 5$	309	369549	0.0008	0.51	7054	9079825	0.0008	2.34
$M_{bb} \in (110.0, 140.0)$ GeV	126	56059	0.0022	0.53	2858	1382411	0.0021	2.43
$M_{ll} \in (80.0, 100.0)$ GeV	107	11674	0.0092	0.99	2456	285269	0.0086	4.59
MET < 30 GeV	91	5472	0.0166	1.23	2026	129095	0.0156	5.62

Table 7: Cut flow and signal significance (z) for the SM $Z(l^+l^-)h(b\bar{b})$ associated production signal with the SM background processes at LHC with $\sqrt{s}=13$ TeV and luminosity of 139 fb^{-1} and at LHC with $\sqrt{s}=14$ TeV and integrated luminosity of 3000 fb^{-1} . Apart, we use the following notations, S: Signal events, B: Background events, S/B: Signal to background ratio.

BPs $(\kappa_Z, c_{uW}, c_{Hq}^{(3)})$	S	B	S/B	z	ϵ_s	ϵ_b
SM (1.00, 0.00, 0.00)	2026	129095	0.0156	5.62	2.09×10^{-2}	8.72×10^{-4}
BP1 (1.00, 0.05, 0.00)	2142		0.0166	5.94	2.19×10^{-2}	
BP2 (1.00, 0.00, 0.05)	2238		0.0173	6.21	2.10×10^{-2}	
BP3 (1.00, 0.00, -0.05)	1869		0.0145	5.19	2.09×10^{-2}	

Table 8: Signal significance of the $Z(l^+l^-)h(b\bar{b})$ production process (at LHC with $\sqrt{s}=14$ TeV and luminosity 3000 fb^{-1}) after the final selection cuts listed in Table 7 for different benchmark points (BPs) in presence of effective operators, along with signal (ϵ_s) and background (ϵ_b) efficiencies.

For signal significance, we use the Asimov definition [78]:

$$z = \sqrt{2 \left((S + B) \ln \left(1 + \frac{S}{B} \right) - S \right)}, \quad (4.1)$$

where S is the number of signal events and B is the number of background events. The Asimov significance is derived from the likelihood ratio, which takes into account the full statistical model, including the Poisson nature of signal and background events. Hence it is more statistically rigorous, not only for small event counts or comparable signal-background scenarios, but also in the general case. On Taylor expansion in the limit $S \ll B$, the Asimov significance approximates to S/\sqrt{B} , which is the more common definition. The number

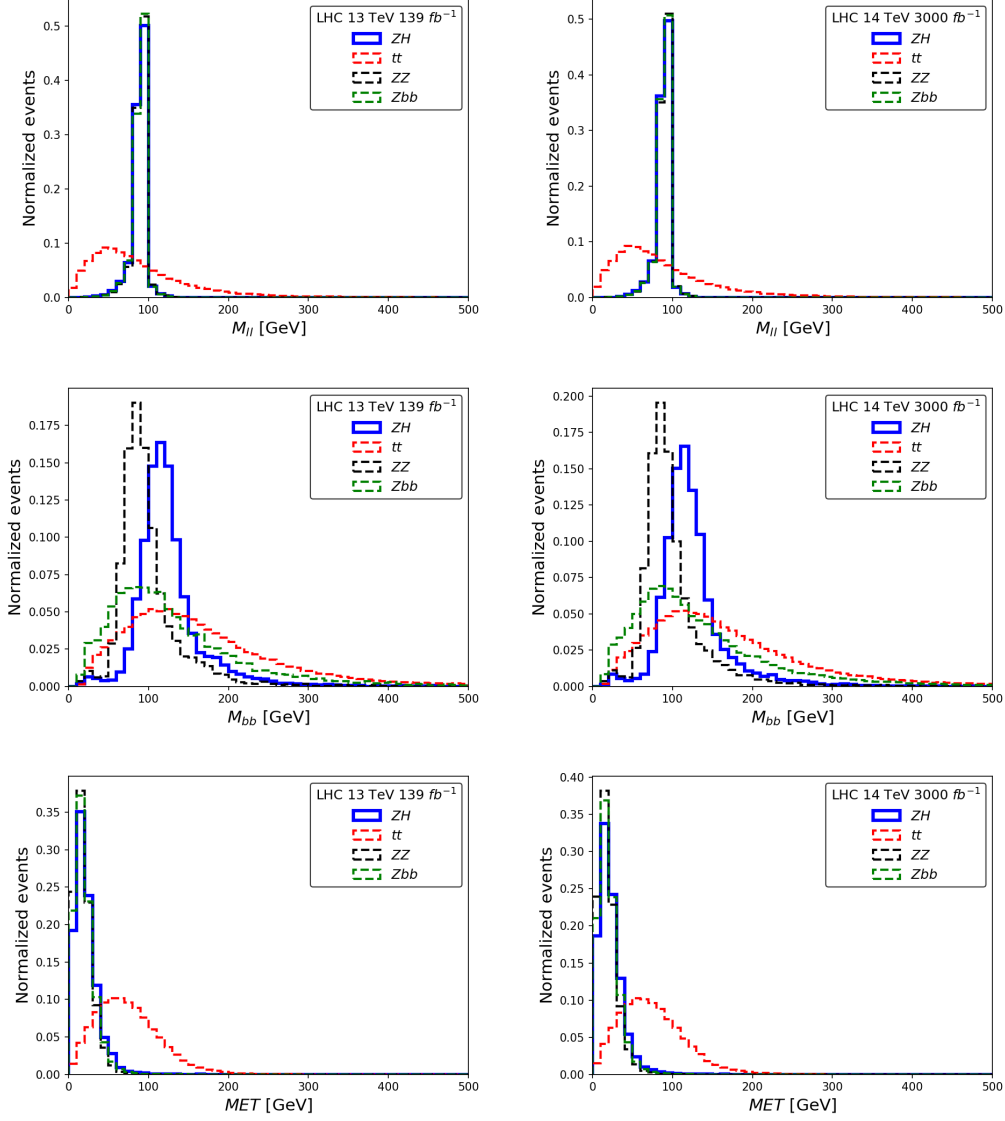


Figure 8: *Top Left:* Invariant mass of dilepton at the LHC 13 TeV corresponding to the SM signal and backgrounds. *Top Right:* Same for LHC 14 TeV. *Middle Left:* Invariant mass of di-bjet at the LHC 13 TeV. *Bottom Left:* Missing transverse energy at the LHC 13 TeV. *Bottom Right:* Same for LHC 14 TeV.

of signal and background events can further be parametrized in terms of the coupling modifiers and the effective operator coefficients as shown in Eqn. 4.2 .

$$\begin{aligned}
S &= \mathcal{L} \times \sigma_{SM+EFT}^S(\kappa_V, c_i) \times BR^S(\kappa_B, c_i) \times \epsilon_S, \\
B &= \mathcal{L} \times \sigma_{SM}^B \times BR^B \times \epsilon_B;
\end{aligned}
\tag{4.2}$$

where, \mathcal{L} is the integrated luminosity, ϵ_S and ϵ_B are the signal and background cut efficiencies respectively. The EFT effects on Z branching to leptons is parametrized in Appendix

D. From Table 7, it is clear that the signal significance improves significantly as we move to the high luminosity frontier.

The second part of the analysis features inclusion of EFT operators. In presence of EFT operators, there is a significant change in the signal significance. This has been illustrated in Table 8 in presence of SMEFT operators at some benchmark values. The relevant kinematic variables and observables for the different benchmark points are shown in Figure 14 of Appendix C. The deviation from the SM signal is minuscule. The benchmarks are chosen at some standard values to gauge the effect on the overall parameter space.

4.2 BDT based analysis

With the advent of modern machine learning tools, multivariate analysis has become a norm in collider analysis [79, 80]. Among the machine learning techniques, boosted decisions trees (BDT) based algorithms are extremely popular due to their stability as well as accuracy even for smaller datasets. With an aim to improved the signal background separation with more accuracy, we perform an analysis using the **XGBoost** classifier [81]. The core setup of the analysis is kept similar to the cut based counterpart. Since, we observed higher significance at 14 TeV, 3000 fb^{-1} LHC, we will perform the BDT based analysis exclusively for the HL-LHC run. The training sets for signal ($pp \rightarrow Z(l^+l^-)H(b\bar{b})$) and backgrounds ($pp \rightarrow t\bar{t}$, $pp \rightarrow ZZ$, $gg \rightarrow Zh$ and $pp \rightarrow Zb\bar{b}$) are prepared and weighted according to its number strength at 3000 fb^{-1} . This weighted data is subjected to the same basic cuts as used in the cut based analysis. The feature selection is done in similar line with the Vh , $h \rightarrow b\bar{b}$ analysis at ATLAS [49]. The features are detailed below:

- Transverse momentum of the leading lepton: p_T^l
- Transverse momentum of the leading b-jet: p_T^b
- Number of jets (inclusive of b-jets): N_j
- Missing transverse energy: MET
- Transverse momentum of the dilepton system: p_T^{ll}
- Transverse momentum of the di-b-jet system: p_T^{bb}
- Invariant mass of the dilepton system: M_{ll}
- Invariant mass of the di-b-jet system: M_{bb}
- Separation in (η, ϕ) space between the leptons: ΔR^{ll}
- Separation in (η, ϕ) space between the b-jets: ΔR^{bb}
- Difference in η between the dilepton and di-b-jet system: $\Delta\eta^{ll,bb}$
- Difference in ϕ between the dilepton and di-b-jet system: $\Delta\phi^{ll,bb}$

The detailed correlation heatmap between the features for signal and backgrounds is shown in Appendix B. To prevent features with large magnitudes (like p_T , MET, etc) to dominate over small valued features (like $\Delta\eta$, ΔR , etc), all the features are scaled about their mean value (\bar{x}) by their standard deviation (SD) i.e. $(x - \bar{x})/SD$. This ensures all features are more or less at equal footing at the beginning of the training process. The signal and background events are divided in 1:1 ratio for training and testing each process. For training, the overall signal weight is equated with the overall background weight ensuring equal number of signal and background events entering the training process. The BDT model is constructed using `XGBClassifier` and the hyperparameter tuning is done using `GridSearchCV` [82]. The details of the optimal hyperparameters is listed in Table 12 in Appendix B. The model is 3 fold cross validated using `StratifiedKfold` [82]. Since, the distributions for the SM plus EFT benchmarks vary very little from the SM distributions, we train only the SM signal and backgrounds and test on the SM as well as on SM plus EFT benchmarks.

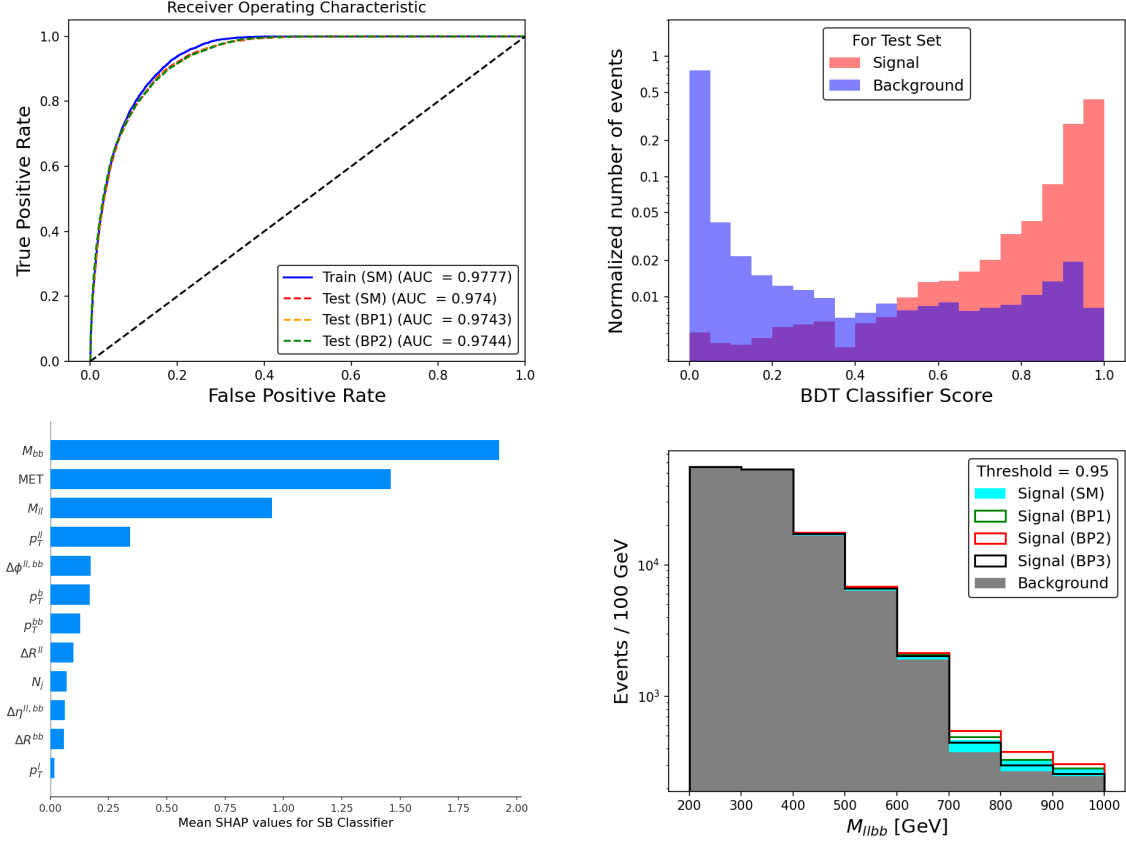


Figure 9: *Top Left:* The Receiver Operating Characteristic (ROC) curve for the training and testing (SM as well as BPs) data. *Top Right:* The distribution of the BDT classifier score for the SM signal and backgrounds. *Bottom Left:* The mean absolute SHAP values for the features used for training the BDT model. *Bottom Right:* M_{llbb} distribution of signal and background processes post threshold selection of 0.95.

The highlights of the BDT analysis are shown in Figure 9. As a metric for evaluation of our model, we use the ROC AUC. The AUC value for the training set is 0.9777. For the test sets, the AUC obtained are 0.9740, 0.9743 and 0.9744 respectively for SM, BP1 and BP2. This indicate that there was very little overfitting and the BPs fared very well on the model trained with SM inputs. To enhance the signal significance, we have set the threshold classifier score at 0.95. This means we will only keep events with a BDT classifier score greater than or equal to 0.95. By doing this, we maintain a roughly similar background efficiency as in the cut-based analysis, making it easier to compare signal efficiencies between the two methods. The feature importance of a machine learning model can be realized using SHAP (SHapley Additive exPlanations) [83] values for the features. SHAP values show how each feature affects each final prediction, the significance of each feature compared to others, and the model’s reliance on the interaction between features. The SHAP values for the model are plotted in Figure 9 using `shap` module. It is distinctly observed that M_{bb} turns out to be the best discriminating feature. MET, M_{ll} and p_T^l turns out to be the other important features which was also taken into account in the cut based analysis. Corresponding to the threshold value of 0.95, the significance and cut efficiencies of the signal and background processes for the BDT analysis are detailed in Table 9. It is observed that for similar background numbers, there is a significant boost in the signal numbers for both SM and other EFT benchmark points, compared to the cut based analysis.

BPs ($\kappa_Z, c_{uW}, c_{Hq}^{(3)}$)	S	B	S/B	z	ϵ_s	ϵ_b
SM (1.00, 0.00, 0.00)	4048	129397	0.0313	11.20	4.17×10^{-2}	8.74×10^{-4}
BP1 (1.00, 0.05, 0.00)	4217		0.0326	11.66	4.33×10^{-2}	
BP2 (1.00, 0.00, 0.05)	4762		0.0368	13.16	4.47×10^{-2}	
BP3 (1.00, 0.00, -0.05)	3484		0.0269	9.64	3.89×10^{-2}	

Table 9: Signal significance of the $Z(l^+l^-)h(b\bar{b})$ production process (at LHC 14 TeV 3000 fb^{-1}) from BDT based analysis (with threshold: 0.95) at different benchmark points (BPs) in presence of effective operators, along with signal (ϵ_s) and background (ϵ_b) efficiencies.

4.3 Two parameter χ^2 analysis

The χ^2 test [2] serves as a statistical measure to evaluate the degree of conformity between empirical observations and theoretical expectations within the framework of a contingency table. In statistical literature, there exist a number of definitions for the χ^2 function. These definitions are more or less equivalent and can be used interchangeably. For our case, we shall use Pearson’s definition where the χ^2 is defined as follows:

$$\chi^2 = \sum_j^{bins} \left(\frac{\mathfrak{D}^j(\kappa_i, c_i) - \mathfrak{D}_{SM}^j}{\Delta N^j(\kappa_i, c_i)} \right)^2 = \sum_j^{bins} \left(\frac{\Delta \mathfrak{D}^j(\kappa_i, c_i)}{\Delta N^j(\kappa_i, c_i)} \right)^2. \quad (4.3)$$

Here, \mathfrak{D} is a differential distribution. For our analysis, $\mathfrak{D} = (d\sigma/dM_{llbb})$, which is the invariant mass of all the visible final state particles following relevant cut/BDT analysis.

We define $\Delta\mathfrak{D}^j(\kappa_i, c_i) = \mathfrak{D}^j(\kappa_i, c_i) - \mathfrak{D}_{SM}^j$, where $\mathfrak{D}^j(\kappa_i, c_i)$ corresponds to events in the j^{th} bin of the M_{lbb} distribution, in presence of effective operators and coupling modifiers and \mathfrak{D}_{SM}^j corresponds to signal events in the same bin under the SM process. $\Delta N^j(\kappa_i, c_i) = \sqrt{\mathfrak{D}^j(\kappa_i, c_i) + \mathfrak{D}_{SM}^j}$ is the statistical uncertainty in the number of events for that bin.

Considering the better performance of the BDT analysis over the cut based analysis, we use the signal and background efficiencies based on the BDT analysis. The χ^2 analysis is performed corresponding to the binned M_{lbb} distribution. The dataset post the threshold cut is divided into 8 bins from 200-1000 GeV in intervals of 100 GeV. The events with higher values of M_{lbb} are removed in order to adhere to the EFT limit. The BDT analysis is repeated for several benchmarks on the parameter space and the distributions corresponding to some of the benchmarks are shown in Appendix C. For a Poisson distributed binned data, the number of degrees of freedom is given by $D = N - M$, where N is the number of bins and M is the number of fitted parameters. In this case, $D = 8 - 2 = 6$. Usually the constraints on the parameter space of physical parameters are reported in terms of confidence levels (C.L.). The confidence levels can be interpreted from the χ^2 values. The 68% and 95% C.L. for $D = 6$ corresponds to $\chi^2 \approx 7.01$ and $\chi^2 \approx 12.59$ respectively. The χ^2 for different parameter benchmarks in $\kappa_Z - \kappa_B$ plane are shown in Figure 10.

Fig. 10 shows that the 68% C.L. bounds are moderately sensitive to the parameter $c_{Hq}^{(3)}$ corresponding to the Higgs-current interaction. This is because $\frac{\sigma}{\sigma_{SM}}$ changes significantly under the variation of $c_{Hq}^{(3)}$ in the Vh channel (see Figure 5 left). However, it requires higher values of c_{uW} to show similar effect in the χ^2 plots. This is mostly due to the fact that the dipole operators contribute at $(1/\Lambda^4)$ order. Further, it should also be noted that the EFT effects can negate each other as evident from the benchmark $\{c_{uW}, c_{Hq}^{(3)}\} = \{0.05, -0.01\}$ (see Figure 10 bottom right) where the positive contribution on the cross section from c_{uW} is cancelled by the negative contribution from $c_{Hq}^{(3)}$ showing negligible deviation from the SM contribution even for non-zero EFT contributions.

The 68% and 95% C.L. bounds on the EFT couplings are shown in Fig. 11, which shows similar sensitivities of the EFT operators and modifiers as in Fig. 11. The effects of EFT contributions to Z decay branching and the assumption of custodial symmetry on these bounds are discussed in Appendix D and Appendix E, respectively. Vh production has been studied in literature like [16, 22] focusing on the boosted regime. However, both these analyses do not consider the light quark dipole operators which we include in our analysis. Considering the boosted regime is interesting as EFT effects are strongly evident there and hence the bounds on $c_{Hq}^{(3)}$ are slightly more stringent in both studies compared to our case. However, as we emphasized in our paper, the boosted regime may invalidate the EFT assumption, necessitating careful consideration. Studies like [18, 23] focus on double differential observables with combination of multiple channels which results in further improvement in bound. Similar to the M_{lbb} distribution, other sensitive observables like H_T (scalar sum of p_T of visible particles) can also be used to perform this analysis. Another popular method is to train a ML based algorithm that separates the SM and SM+EFT contribution based on a set of discriminating observables. However, such model requires better segregation between the observables of the two classes which is

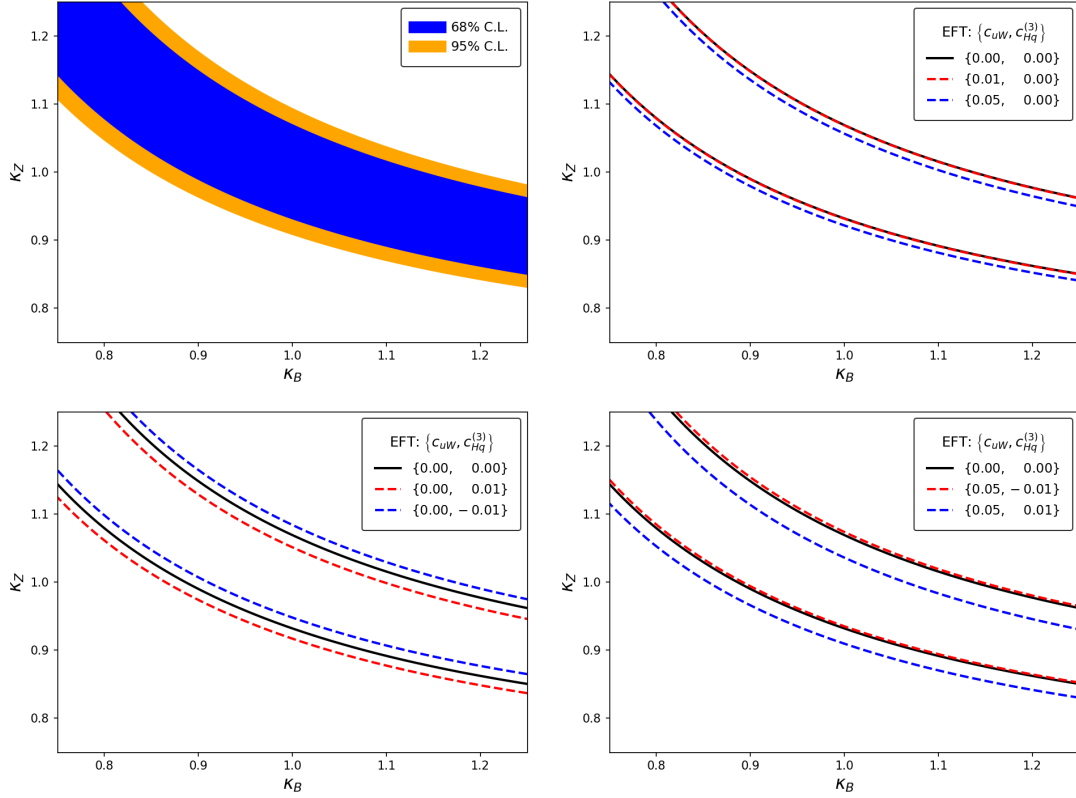


Figure 10: *Top Left:* χ^2 plots showing 68% C.L. and 95% bounds in the $\kappa_Z - \kappa_B$ space at LHC 14 TeV 3000 fb^{-1} . *Top Right, Bottom Left and Bottom Right:* Shift in 68% C.L. bounds for different values of effective coefficients.

evidently difficult even at HL-LHC once we abide by the EFT limit.

4.4 Other future pp colliders

As observed in Fig. 2 and 3, the Zh production cross section enhances for both the Higgs-current and dipole interactions, with increase in CoM energy. This motivates the possibility of better extraction of these NP contributions at higher CoM energy possible at future collider runs like the HE-LHC (expected to run at $\sqrt{s} = 27$ TeV), FCC-hh (expected to run at $\sqrt{s} = 100$ TeV), etc. $\frac{\sigma}{\sigma_{SM}}$ is plotted in Fig. 12 (left) for different CoM energies (\sqrt{s}) at some of the benchmarks $\{c_{uW}, c_{Hq}^{(3)}\}$: BP1 $\{0.05, 0.00\}$, BP2 $\{0.00, 0.05\}$ and BP3 $\{0.05, 0.05\}$. All the benchmarks show enhancement in EFT effects, however we observe stronger enhancement for the Higgs-current interaction (BP2) in comparison to the dipole interaction (BP1). The combined presence of both the operators (BP3) shows the highest enhancement in cross-section. While these results show promise to better estimate the dipole operator in particular, the prospect of accelerating protons to such high energies remains a distant possibility. Fig. 12 (right) shows the validity of EFT limit, having the invariant mass peak well below $\Lambda = 1$ TeV even in context of future pp colliders with higher CoM energies. This happens due to the dominance of SM process, while larger

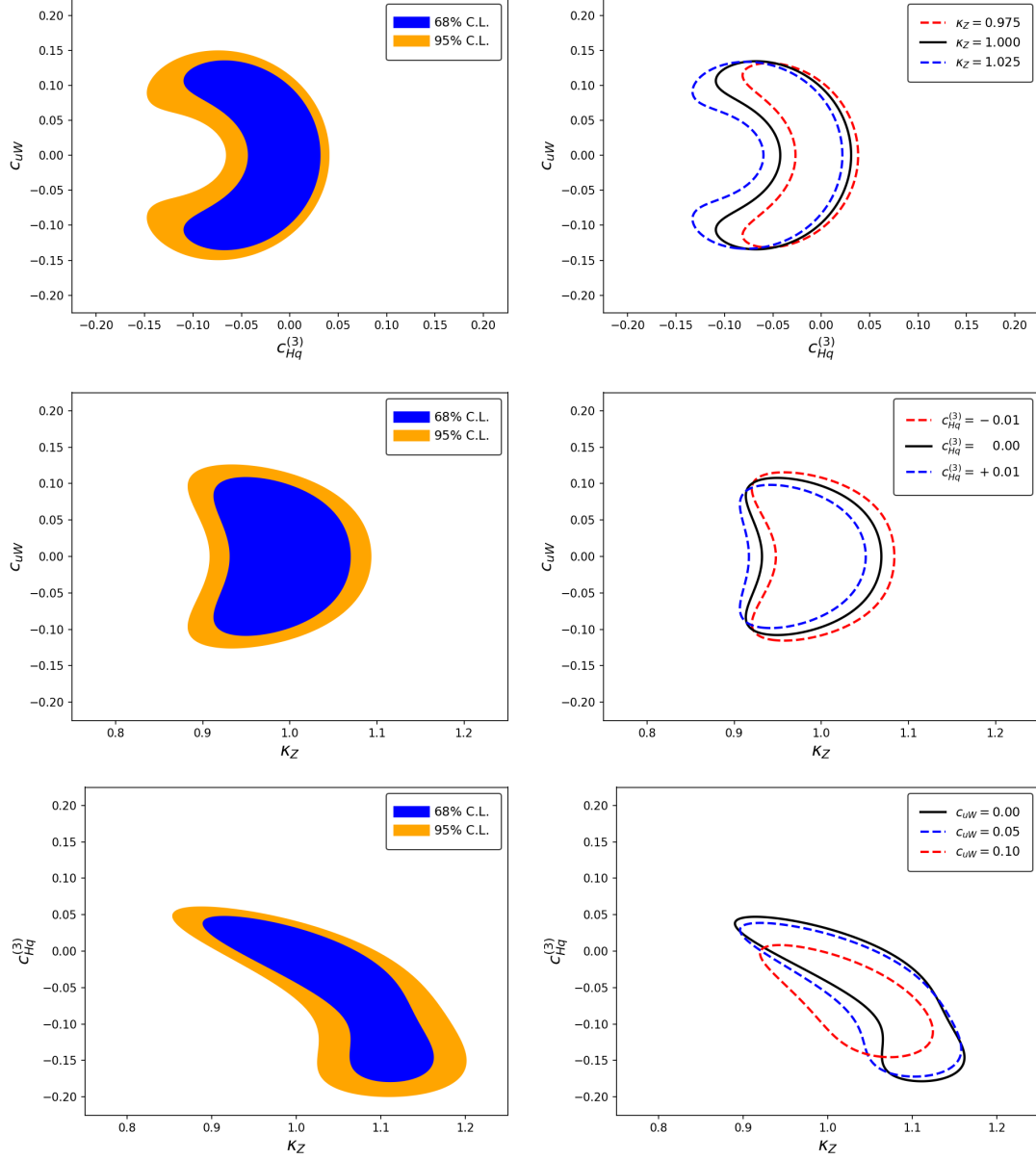


Figure 11: *Top Left, Middle Left and Bottom Left:* 68% and 95% C.L. bounds on effective coefficients at the 14 TeV 3000 fb^{-1} LHC. *Top Right, Middle Right and Bottom Right:* Shift in 68% C.L. in presence of different modifiers or EFT coefficients.

Wilson coefficient would flatten the distribution having more events with higher invariant mass.

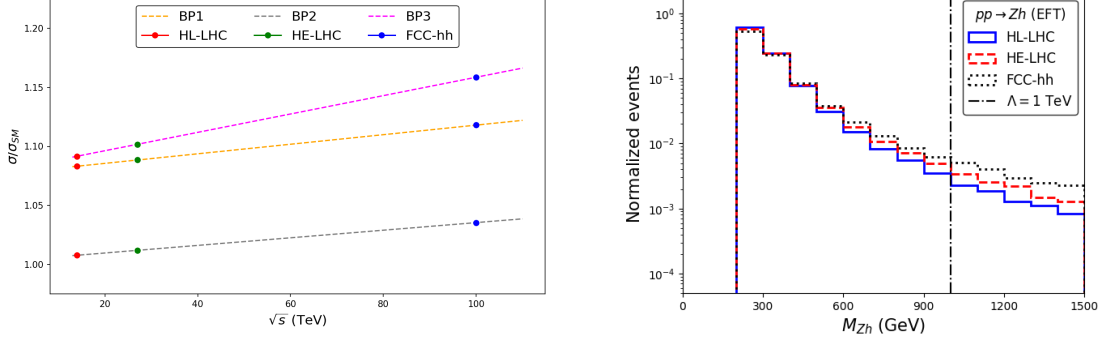


Figure 12: *Left:* Variation in the ratio of Zh production cross section to the SM cross section at different CoM energies for benchmarks $\{c_{uW}, c_{Hq}^{(3)}\}$: BP1 $\{0.05, 0.00\}$, BP2 $\{0.00, 0.05\}$ and BP3 $\{0.05, 0.05\}$. *Right:* Invariant mass of Zh for the parton level processes in presence of EFT operators at BP3 for different future pp collider runs.

5 Summary and conclusion

We have presented an analysis of Zh associated production at the LHC in presence of dimension six SMEFT operators and coupling modifiers. We choose a simple parametrisation to match the coupling modifiers that stem from dimension six SMEFT operators in Warsaw basis. We analysed the signal and background contributions at various benchmark points, which allows maximum cross-section within the allowed values of the EFT parameters and coupling modifiers adhering to the constraints appearing from existing collider and flavour constraints. We do both cut-based and BDT analysis using kinematic variables relevant for the process. NP scale is safely chosen at $\Lambda = 1$ TeV, which abides by the effective limit having invariant mass distribution peak appearing below Λ .

A comparison of Table 8 and 9 shows that the BDT analysis perform better than the cut based analysis presented in previous section as expected. One obtains almost factor 2 enhancement in the estimation of the significances for the various BP's considered in our analysis. This is due to the fact that BDT comes with better efficiency for the signal events even though the background efficiency remains almost the same. We have obtained more than 9σ (5σ) significance using BDT (cut based) analysis for all our chosen benchmark points. We further note that corresponding to our flavor scheme choice $(U(2)_q \times U(2)_u \times U(2)_d)$ the corresponding background contributions have limited sensitivity to the EFT operators introduced here, hence we do not include them in our analysis.

A χ^2 analysis is performed in the two dimensional parameter space of the EFT operator coefficients as well as in the coupling modifiers. The bounds on the $c_{uW} - c_{Hq}^{(3)}$ plane is more constrained than those on $\kappa_Z - \kappa_B$ plane, owing to the fact that the differential distribution M_{llbb} is extremely sensitive to EFT effects especially at the tail. Based on the plots in Figure 10, it is evident that the EFT contributions significantly alters the

bounds on the $\kappa_Z - \kappa_B$ plane. Similarly, coupling modifiers can also impact the bounds in the EFT coefficient planes as evident from Figure 11. It is observed that even with the tight constraints on the operators, presence of Higgs-current operator $\mathcal{O}_{Hq}^{(3)}$ results in visible changes on the bounds in $\kappa_Z - \kappa_B$ plane. The individual impact of the dipole operator \mathcal{O}_{uW} is relatively small and do not show any significant deviation from the SM predictions. This is mainly because, they do not interfere with the SM process and the contributions are obtained only at $1/\Lambda^4$ order. However, as discussed in section 4.4, significant increase in sensitivity is expected with increase in the CoM energy, possible at future high energy collider runs. However, the contributions from $\mathcal{O}_{Hq}^{(3)}$ will still dominate.

In this analysis, we have omitted CP odd contributions to the dipole operators, primarily because they are strongly bounded from EDM measurements. Therefore, it is difficult to detect their effects via signal cross-section. Dedicated CP violating observables may decipher a disentanglement from that of a CP even case. This lies outside the scope of the present work, but will be taken up in future.

Acknowledgments

Subhaditya would like to acknowledge the grant CRG/2019/004078 from DST-SERB, Govt. of India.

A Constraints on operators

The constraints on dipole (other than c_{uW}) and Higgs-current (other than $c_{Hq}^{(3)}$) operator coefficients from existing studies are listed in Table 10 and 11, respectively.

Coefficient	Bound	C.L.	Flavor Scheme [Source]
c_{uB}	[-0.602, 0.602]	95%	$U(3)_q \times U(3)_u \times U(3)_d$ [64]
	[-0.780, 0.780]	95%	$U(2)_q \times U(2)_u \times U(2)_d$ [65]
	[-0.199, 0.093]	95%	$U(1)_Q \times U(1)_t$ [50]
	[-0.036, 0.324]	90%	$U(3)_q \times U(3)_u \times U(3)_d$ [56]
	[-0.430, 0.284]	95%	$U(1)_Q \times U(1)_t$ [54]
	[-4.500, 1.200]	95%	$U(1)_Q \times U(1)_t$ [51]
c_{dW}	[-0.484, 0.484]	95%	$U(3)_q \times U(3)_u \times U(3)_d$ [64]
	[-0.360, 0.360]	95%	$U(2)_q \times U(2)_u \times U(2)_d$ [65]
c_{dB}	[-0.769, 0.769]	95%	$U(3)_q \times U(3)_u \times U(3)_d$ [64]
	[-0.960, 0.960]	95%	$U(2)_q \times U(2)_u \times U(2)_d$ [65]

Table 10: Constraints on dipole operator coefficients from existing studies, see the references for details.

Bounds on the imaginary part of dipole operators from neutron EDM [67] (assuming

Coefficient	Bound	C.L.	Flavor Scheme [Source]
$c_{Hq}^{(1)}$	[-2.659, 0.381]	95%	$U(2)_q \times U(2)_u \times U(3)_d$ [50]
	[-1.147, 1.585]	95%	$U(1)_Q \times U(1)_t$ [50]
	[-0.260, 0.115]	68%	$U(3)_q \times U(3)_u \times U(3)_d$ [57]
	[-1.600, 0.430]	95%	$U(3)_q \times U(3)_u \times U(3)_d$ [58]
	[-0.048, 0.021]	90%	$U(3)_q \times U(3)_u \times U(3)_d$ [56]
	[-0.100, 0.140]	95%	$U(2)_q \times U(2)_u \times U(3)_d$ [51]
	[-0.031, 0.049]	95%	$U(1)_Q \times U(1)_t$ [51]
	[-0.023, 0.047]	95%	$U(2)_q \times U(2)_u \times U(3)_d$ [53]
c_{Hu}	[-0.458, 0.375]	95%	$U(2)_q \times U(2)_u \times U(3)_d$ [50]
	[-1.038, 0.449]	68%	$U(3)_q \times U(3)_u \times U(3)_d$ [57]
	[-0.060, 0.036]	90%	$U(3)_q \times U(3)_u \times U(3)_d$ [56]
	[-0.190, 0.100]	68%	$U(3)_q \times U(3)_u \times U(3)_d$ [49]
	[-0.075, 0.073]	95%	$U(2)_q \times U(2)_u \times U(3)_d$ [51]
	[-1.200, 2.900]	95%	$U(1)_Q \times U(1)_t$ [51]
	[-0.056, 0.081]	95%	$U(2)_q \times U(2)_u \times U(3)_d$ [53]
c_{Hd}	[-0.187, 0.229]	95%	$U(2)_q \times U(2)_u \times U(3)_d$ [50]
	[-0.520, 0.267]	68%	$U(3)_q \times U(3)_u \times U(3)_d$ [57]
	[-2.600, 8.300]	95%	$U(3)_q \times U(3)_u \times U(3)_d$ [58]
	[-0.130, 0.071]	95%	$U(2)_q \times U(2)_u \times U(3)_d$ [51]
	[-0.150, 0.040]	95%	$U(2)_q \times U(2)_u \times U(3)_d$ [53]

Table 11: Constraints on Higgs-current operator coefficients from existing studies, see the references for details.

$U(2)_q \times U(2)_u \times U(2)_d$ flavor scheme) are shown below:

$$\begin{aligned}
\Im(c_{uB}) &< 0.000368 \\
\Im(c_{dW}) &< 0.000002 \\
\Im(c_{dB}) &< 0.000001
\end{aligned} \tag{A.1}$$

B Details of BDT analysis

Feature selection is an integral and significant part of any machine learning analysis. Presence of too many redundant features causes a model to learn unnecessary characteristics, as such we expect the features to have little dependence on one another. The correlation matrix captures the interdependence among the features very accurately. For our BDT model, the feature correlation heatmap is shown in Figure 13. Darker patches refer to high correlation. Apart from features like p_T^l and p_T^l , p_T^b and p_T^{bb} , where correlation is expected, most of the features show little to no correlation, enhancing the model’s learnability against general data. Apart from feature selection, another important aspect of model tuning is the hyperparameter optimization. Proper tuning prevents the model from overfitting, resulting in better performance on new data. The optimized hyperparameters for the model are detailed in Table 12.

Hyperparameters for the XGBClassifier model	Optimal value
Number of boosting rounds (<code>n_estimators</code>)	50
Maximum depth of a tree (<code>max_depth</code>)	5
Learning rate for the model (<code>learning_rate</code>)	0.15
Fraction of samples used each tree (<code>subsample</code>)	0.8
Fraction of features used for each tree (<code>colsample_bytree</code>)	1.0
Minimum sum of instance weight in a child (<code>min_child_weight</code>)	50
Minimum loss reduction for further partition (<code>gamma</code>)	0.75
L1 regularization term on weights (<code>reg_alpha</code>)	8
L2 regularization term on weights (<code>reg_lambda</code>)	60
Maximum step size for each iteration (<code>max_delta_step</code>)	2

Table 12: The optimal hyperparameter values for the model mined using GridSearchCV. The objective hyperparameter is fixed at "binary:logistic".

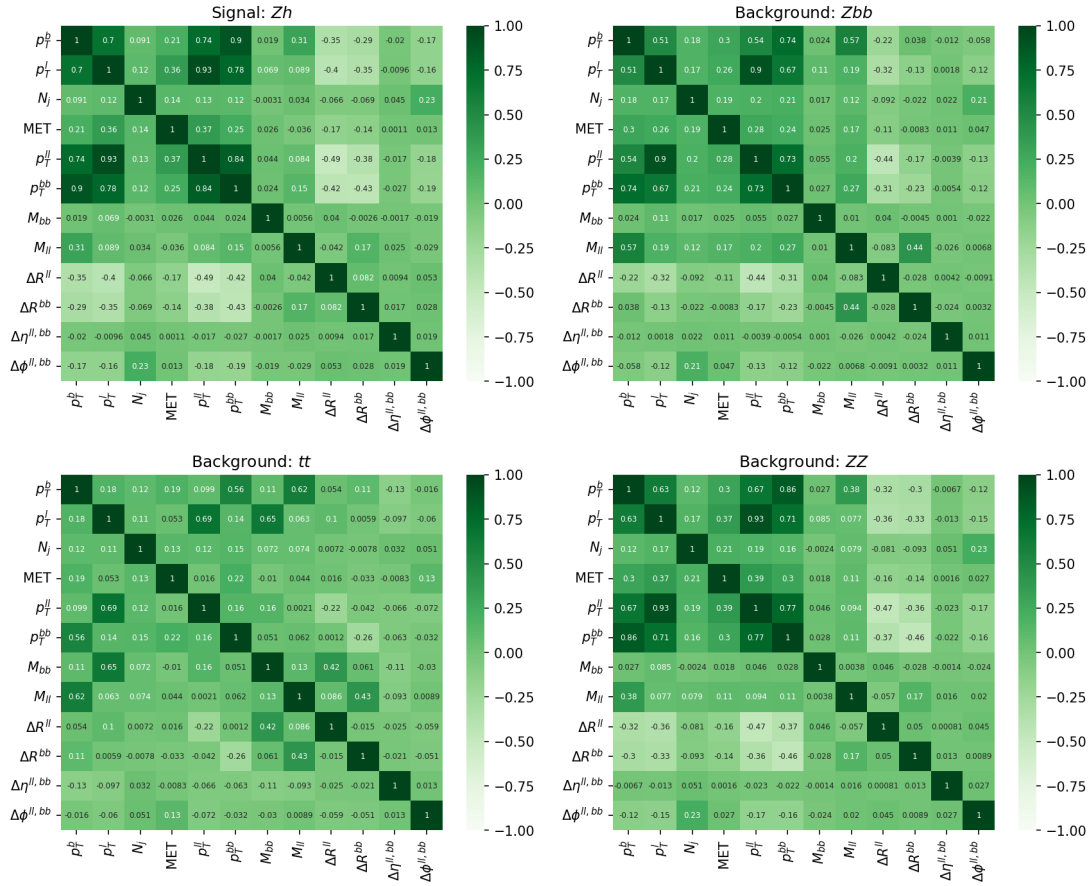


Figure 13: Top Left: Correlation matrix for the features used in training the XGBoost model for Zh process. Top Right: Zbb process. Bottom Left: $t\bar{t}$ process. Bottom Right: ZZ process.

C Differential distributions

Kinematic distributions for different EFT benchmark points are shown in Figure 14. The M_{llbb} distribution post BDT score threshold choice of 0.95 are shown in Figure 15.

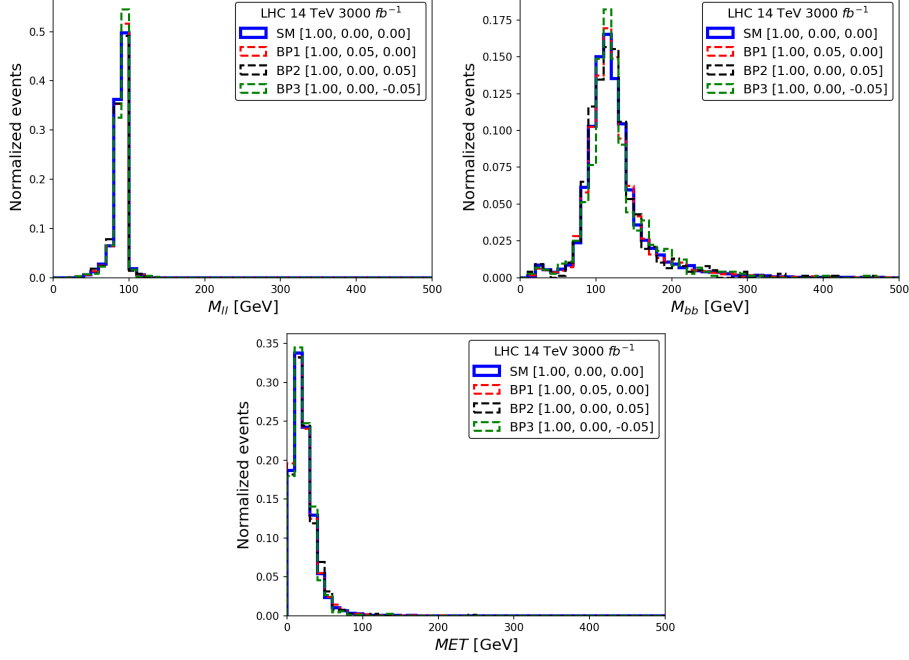


Figure 14: *Top Left:* Invariant mass of dilepton, *Top Right:* invariant mass of di-bjet and *Bottom:* missing transverse energy corresponding to $Z(l^+l^-)h(b\bar{b})$ at $\sqrt{s}=14$ TeV at different EFT benchmark points shown in Table 8.

The benchmarks $\{c_{uW}, c_{Hq}^{(3)}\}$ are: *Left:* BC1 $\{0.00, -0.20\}$, BC2 $\{0.00, -0.10\}$ and BC3 $\{0.00, -0.01\}$; *Center:* BC4 $\{0.00, 0.01\}$, BC5 $\{0.00, 0.10\}$ and BC6 $\{0.00, 0.20\}$; *Right:* BD1 $\{0.01, 0.00\}$, BD2 $\{0.10, 0.00\}$ and BD3 $\{0.20, 0.00\}$.

D Z branching correction

The correction to Z decay width in presence of \mathcal{O}_{uW} and $\mathcal{O}_{Hq}^{(3)}$ can be parametrized as:

$$\Gamma_Z = \Gamma_Z^{SM} \left[1 + 0.0047 (c_{uW})^2 + 0.0099 (c_{Hq}^{(3)})^2 + 0.0976 (c_{Hq}^{(3)}) \right] \quad (D.1)$$

The correction to $Z \rightarrow l^+l^-$ branching is $\mathcal{O}_{Hq}^{(3)}$ can be parametrized as:

$$(B.R.)_{Zl} = \frac{\Gamma_{Zl}}{\Gamma_Z} = \frac{(B.R.)_{Zl}^{SM}}{\left[1 + 0.0047 (c_{uW})^2 + 0.0099 (c_{Hq}^{(3)})^2 + 0.0976 (c_{Hq}^{(3)}) \right]} \quad (D.2)$$

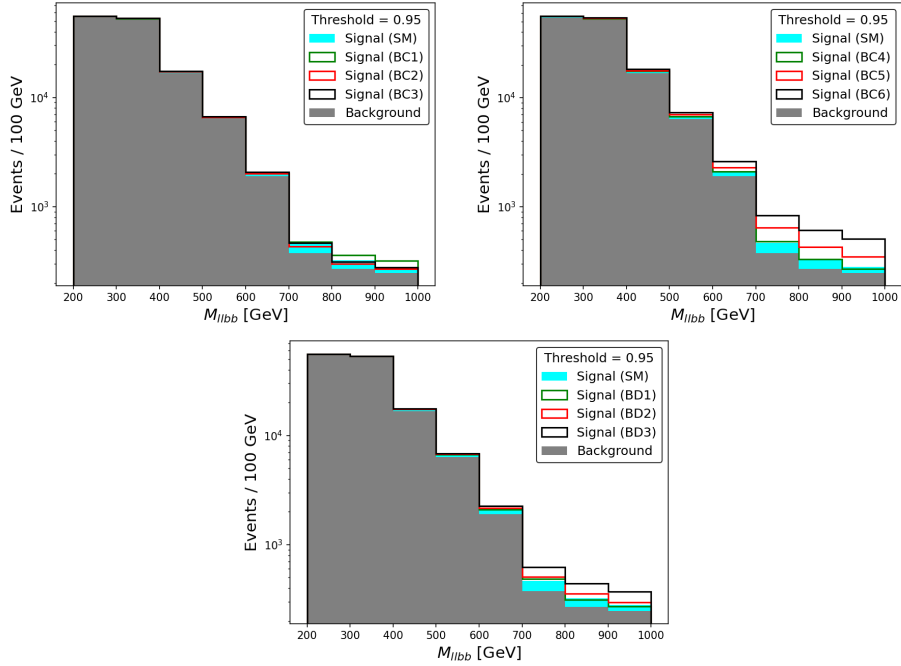


Figure 15: M_{llbb} distributions for different EFT benchmarks post threshold choice of 0.95.

Figure 16 shows how the 68% C.L. limits change depending on whether EFT corrections to the Z branching are included or not. The effect is not very strong, but it is taken into account in our analysis.

E The effect of custodial symmetry

In Section 3, we imposed the custodial symmetry condition $\kappa_W = \kappa_Z$. However, this assumption can be relaxed. In this section, we explore how the 68% C.L. limits change under two scenarios: (i) with custodial symmetry, where $\kappa_W = \kappa_Z$ (as discussed in Section 3), and (ii) without custodial symmetry, where $\kappa_W \neq \kappa_Z$ and $\kappa_W = 1$, assuming an SM-like coupling of the Higgs to the W boson while treating κ_Z as a free parameter. For the second scenario, the Higgs production signal strength via the Zh channel is given by:

$$\mu_{hh}^{Zh} = \frac{(\sigma^{Zh} \times (B.R.)_{hh})}{(\sigma^{Zh} \times (B.R.)_{hh})_{SM}} = \frac{\kappa_Z^2 \kappa_B^2}{0.3929 + 0.5809 \kappa_B^2 + 0.0262 \kappa_Z^2}, \quad (\text{E.1})$$

Figure 17 illustrates how the 68% C.L. limits are affected by the assumption of custodial symmetry. The assumption significantly impacts our bounds, particularly when κ_Z deviates from 1.

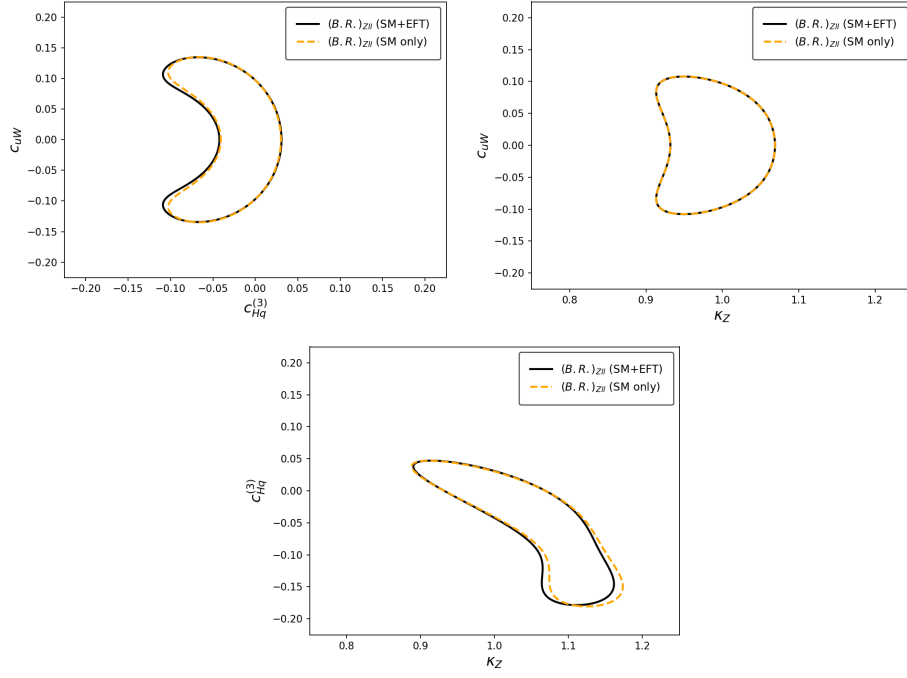


Figure 16: Shift in 68% C.L. limits depending on whether EFT corrections to the Z branching are included or not.

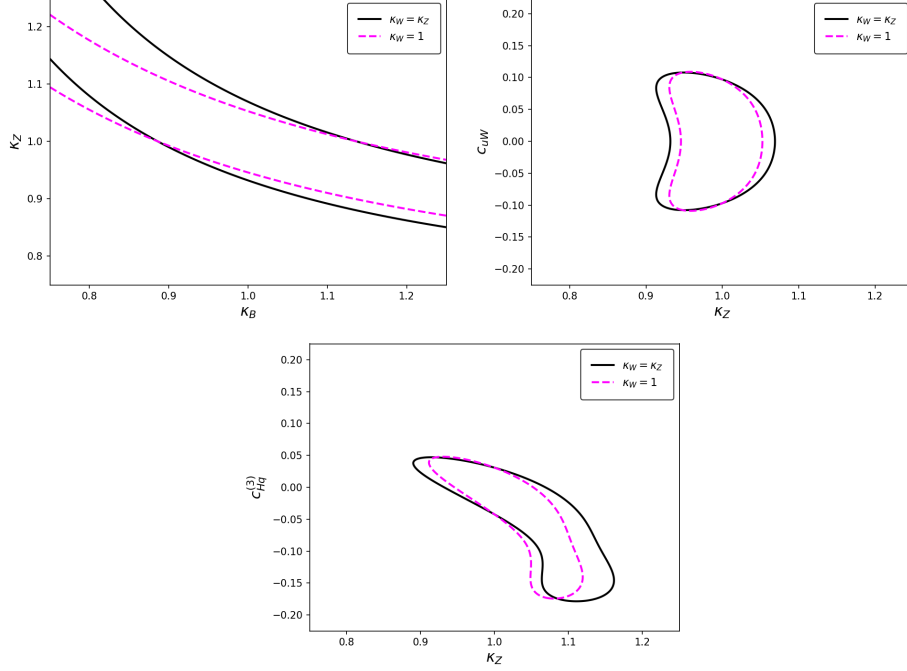


Figure 17: Shift in 68% C.L. limits depending on whether custodial symmetry is assumed.

References

- [1] H.E. Logan, *TASI 2013 lectures on Higgs physics within and beyond the Standard Model*, [1406.1786](#).
- [2] PARTICLE DATA GROUP collaboration, *Review of Particle Physics*, *PTEP* **2022** (2022) [083C01](#).
- [3] ATLAS collaboration, *A detailed map of Higgs boson interactions by the ATLAS experiment ten years after the discovery*, *Nature* **607** (2022) 52 [[2207.00092](#)].
- [4] CMS collaboration, *A portrait of the Higgs boson by the CMS experiment ten years after the discovery.*, *Nature* **607** (2022) 60 [[2207.00043](#)].
- [5] CMS collaboration, *Constraints on anomalous HVV couplings from the production of Higgs bosons decaying to τ lepton pairs*, *Phys. Rev. D* **100** (2019) 112002 [[1903.06973](#)].
- [6] I. Anderson et al., *Constraining Anomalous HVV Interactions at Proton and Lepton Colliders*, *Phys. Rev. D* **89** (2014) 035007 [[1309.4819](#)].
- [7] P. Sharma and A. Shivaji, *Probing non-standard HVV ($V = W, Z$) couplings in single Higgs production at future electron-proton collider*, *JHEP* **10** (2022) 108 [[2207.03862](#)].
- [8] A.I. Hernández-Juárez, G. Tavares-Velasco and A. Fernández-Téllez, *New evaluation of the HZZ coupling: Direct bounds on anomalous contributions and CP-violating effects via a new asymmetry*, *Phys. Rev. D* **107** (2023) 115031 [[2301.13127](#)].
- [9] S. Dutta, K. Hagiwara and Y. Matsumoto, *Measuring the Higgs-Vector boson Couplings at Linear e^+e^- Collider*, *Phys. Rev. D* **78** (2008) 115016 [[0808.0477](#)].
- [10] N. Desai, D.K. Ghosh and B. Mukhopadhyaya, *CP-violating HWW couplings at the Large Hadron Collider*, *Phys. Rev. D* **83** (2011) 113004 [[1104.3327](#)].
- [11] N.D. Christensen, T. Han and Y. Li, *Testing CP Violation in ZZH Interactions at the LHC*, *Phys. Lett. B* **693** (2010) 28 [[1005.5393](#)].
- [12] S. Dwivedi, D.K. Ghosh, B. Mukhopadhyaya and A. Shivaji, *Distinguishing CP-odd couplings of the Higgs boson to weak boson pairs*, *Phys. Rev. D* **93** (2016) 115039 [[1603.06195](#)].
- [13] F.U. Bernlochner, C. Englert, C. Hays, K. Lohwasser, H. Mildner, A. Pilkington et al., *Angles on CP-violation in Higgs boson interactions*, *Phys. Lett. B* **790** (2019) 372 [[1808.06577](#)].
- [14] J. Brehmer, F. Kling, T. Plehn and T.M.P. Tait, *Better Higgs-CP Tests Through Information Geometry*, *Phys. Rev. D* **97** (2018) 095017 [[1712.02350](#)].
- [15] S. Banerjee, T. Mandal, B. Mellado and B. Mukhopadhyaya, *Cornering dimension-6 HVV interactions at high luminosity LHC: the role of event ratios*, *JHEP* **09** (2015) 057 [[1505.00226](#)].
- [16] S. Banerjee, C. Englert, R.S. Gupta and M. Spannowsky, *Probing Electroweak Precision Physics via boosted Higgs-strahlung at the LHC*, *Phys. Rev. D* **98** (2018) 095012 [[1807.01796](#)].
- [17] S. Banerjee, R.S. Gupta, J.Y. Reiness and M. Spannowsky, *Resolving the tensor structure of the Higgs coupling to Z-bosons via Higgs-strahlung*, *Phys. Rev. D* **100** (2019) 115004 [[1905.02728](#)].

- [18] S. Banerjee, R.S. Gupta, J.Y. Reiness, S. Seth and M. Spannowsky, *Towards the ultimate differential SMEFT analysis*, *JHEP* **09** (2020) 170 [[1912.07628](#)].
- [19] F.F. Freitas, C.K. Khosa and V. Sanz, *Exploring the standard model EFT in VH production with machine learning*, *Phys. Rev. D* **100** (2019) 035040 [[1902.05803](#)].
- [20] F. Bishara, P. Englert, C. Grojean, G. Panico and A.N. Rossia, *Revisiting $Vh(\rightarrow b\bar{b})$ at the LHC and FCC-hh*, *JHEP* **06** (2023) 077 [[2208.11134](#)].
- [21] F. Bishara, S. De Curtis, L. Delle Rose, P. Englert, C. Grojean, M. Montull et al., *Precision from the diphoton Zh channel at FCC-hh*, *JHEP* **04** (2021) 154 [[2011.13941](#)].
- [22] P. Englert, *Improved Precision in $Vh(\rightarrow b\bar{b})$ via Boosted Decision Trees*, [2407.21239](#).
- [23] S. Banerjee, R.S. Gupta, O. Ochoa-Valeriano, M. Spannowsky and E. Venturini, *A fully differential SMEFT analysis of the golden channel using the method of moments*, *JHEP* **06** (2021) 031 [[2012.11631](#)].
- [24] S. Banerjee, R.S. Gupta, O. Ochoa-Valeriano and M. Spannowsky, *High energy lepton colliders as the ultimate Higgs microscopes*, *JHEP* **02** (2022) 176 [[2109.14634](#)].
- [25] T. Biswas, A. Datta and B. Mukhopadhyaya, *Following the trail of new physics via the vector boson fusion Higgs boson signal at the Large Hadron Collider*, *Phys. Rev. D* **105** (2022) 055028 [[2107.05503](#)].
- [26] J.Y. Araz, S. Banerjee, R.S. Gupta and M. Spannowsky, *Precision SMEFT bounds from the VBF Higgs at high transverse momentum*, *JHEP* **04** (2021) 125 [[2011.03555](#)].
- [27] H.T. Li, B. Yan and C.P. Yuan, *Discriminating between Higgs Production Mechanisms via Jet Charge at the LHC*, *Phys. Rev. Lett.* **131** (2023) 041802 [[2301.07914](#)].
- [28] B. Yan, *Determining Higgs boson width at electron-positron colliders*, *Phys. Lett. B* **822** (2021) 136709 [[2105.04530](#)].
- [29] K.-P. Xie and B. Yan, *Probing the electroweak symmetry breaking with Higgs production at the LHC*, *Phys. Lett. B* **820** (2021) 136515 [[2104.12689](#)].
- [30] I. Brivio and M. Trott, *The Standard Model as an Effective Field Theory*, *Phys. Rept.* **793** (2019) 1 [[1706.08945](#)].
- [31] Q. Bonnefoy, J. Kley, D. Liu, A.N. Rossia and C.-Y. Yao, *Aligned Yet Large Dipoles: a SMEFT Study*, [2403.13065](#).
- [32] R. Alonso, E.E. Jenkins and A.V. Manohar, *A Geometric Formulation of Higgs Effective Field Theory: Measuring the Curvature of Scalar Field Space*, *Phys. Lett. B* **754** (2016) 335 [[1511.00724](#)].
- [33] A. Crivellin, M. Ghezzi and M. Procura, *Effective Field Theory with Two Higgs Doublets*, *JHEP* **09** (2016) 160 [[1608.00975](#)].
- [34] Anisha, S. Das Bakshi, J. Chakraborty and S. Prakash, *Hilbert Series and Plethystics: Paving the path towards 2HDM- and MLRSM-EFT*, *JHEP* **09** (2019) 035 [[1905.11047](#)].
- [35] F. del Aguila, S. Bar-Shalom, A. Soni and J. Wudka, *Heavy Majorana Neutrinos in the Effective Lagrangian Description: Application to Hadron Colliders*, *Phys. Lett. B* **670** (2009) 399 [[0806.0876](#)].
- [36] A. Aparici, K. Kim, A. Santamaria and J. Wudka, *Right-handed neutrino magnetic moments*, *Phys. Rev. D* **80** (2009) 013010 [[0904.3244](#)].

- [37] S. Bhattacharya and J. Wudka, *Dimension-seven operators in the standard model with right handed neutrinos*, *Phys. Rev. D* **94** (2016) 055022 [[1505.05264](#)].
- [38] Y. Liao and X.-D. Ma, *Operators up to Dimension Seven in Standard Model Effective Field Theory Extended with Sterile Neutrinos*, *Phys. Rev. D* **96** (2017) 015012 [[1612.04527](#)].
- [39] H.-L. Li, Z. Ren, J. Shu, M.-L. Xiao, J.-H. Yu and Y.-H. Zheng, *Complete set of dimension-eight operators in the standard model effective field theory*, *Phys. Rev. D* **104** (2021) 015026 [[2005.00008](#)].
- [40] C.W. Murphy, *Dimension-8 operators in the Standard Model Effective Field Theory*, *JHEP* **10** (2020) 174 [[2005.00059](#)].
- [41] B. Grzadkowski, M. Iskrzynski, M. Misiak and J. Rosiek, *Dimension-Six Terms in the Standard Model Lagrangian*, *JHEP* **10** (2010) 085 [[1008.4884](#)].
- [42] S. Bhattacharya and J. Wudka, *Effective theories with dark matter applications*, *Int. J. Mod. Phys. D* **30** (2021) 2130004 [[2104.01788](#)].
- [43] A. Alloul, N.D. Christensen, C. Degrande, C. Duhr and B. Fuks, *FeynRules 2.0 - A complete toolbox for tree-level phenomenology*, *Comput. Phys. Commun.* **185** (2014) 2250 [[1310.1921](#)].
- [44] C. Degrande, C. Duhr, B. Fuks, D. Grellscheid, O. Mattelaer and T. Reiter, *UFO - The Universal FeynRules Output*, *Comput. Phys. Commun.* **183** (2012) 1201 [[1108.2040](#)].
- [45] I. Brivio, *SMEFTsim 3.0 — a practical guide*, *JHEP* **04** (2021) 073 [[2012.11343](#)].
- [46] C. Degrande, G. Durieux, F. Maltoni, K. Mimasu, E. Vryonidou and C. Zhang, *Automated one-loop computations in the standard model effective field theory*, *Phys. Rev. D* **103** (2021) 096024 [[2008.11743](#)].
- [47] J. Alwall, M. Herquet, F. Maltoni, O. Mattelaer and T. Stelzer, *MadGraph 5 : Going Beyond*, *JHEP* **06** (2011) 128 [[1106.0522](#)].
- [48] CMS collaboration, *Observation of Higgs boson decay to bottom quarks*, *Phys. Rev. Lett.* **121** (2018) 121801 [[1808.08242](#)].
- [49] ATLAS collaboration, *Measurements of WH and ZH production in the $H \rightarrow b\bar{b}$ decay channel in pp collisions at 13 TeV with the ATLAS detector*, *Eur. Phys. J. C* **81** (2021) 178 [[2007.02873](#)].
- [50] SMEFT collaboration, *Combined SMEFT interpretation of Higgs, diboson, and top quark data from the LHC*, *JHEP* **11** (2021) 089 [[2105.00006](#)].
- [51] J. Ellis, M. Madigan, K. Mimasu, V. Sanz and T. You, *Top, Higgs, Diboson and Electroweak Fit to the Standard Model Effective Field Theory*, *JHEP* **04** (2021) 279 [[2012.02779](#)].
- [52] I. Brivio, S. Bruggisser, N. Elmer, E. Geoffray, M. Luchmann and T. Plehn, *To profile or to marginalize - A SMEFT case study*, *SciPost Phys.* **16** (2024) 035 [[2208.08454](#)].
- [53] Anisha, S. Das Bakshi, S. Banerjee, A. Biekötter, J. Chakraborty, S. Kumar Patra et al., *Effective limits on single scalar extensions in the light of recent LHC data*, *Phys. Rev. D* **107** (2023) 055028 [[2111.05876](#)].
- [54] A. Buckley, C. Englert, J. Ferrando, D.J. Miller, L. Moore, M. Russell et al., *Constraining top quark effective theory in the LHC Run II era*, *JHEP* **04** (2016) 015 [[1512.03360](#)].
- [55] S. Bißmann, C. Grunwald, G. Hiller and K. Kröninger, *Top and Beauty synergies in SMEFT-fits at present and future colliders*, *JHEP* **06** (2021) 010 [[2012.10456](#)].

- [56] C. Grunwald, G. Hiller, K. Kröninger and L. Nollen, *More synergies from beauty, top, Z and Drell-Yan measurements in SMEFT*, *JHEP* **11** (2023) 110 [[2304.12837](#)].
- [57] M. Thomas Arun, K. Deka and T. Srivastava, *Constraining SMEFT BSM scenarios with EWPO and Δ_{CKM}* , [2301.09273](#).
- [58] ATLAS collaboration, *Measurements of differential cross-sections in four-lepton events in 13 TeV proton-proton collisions with the ATLAS detector*, *JHEP* **07** (2021) 005 [[2103.01918](#)].
- [59] ATLAS collaboration, *Combined measurements of Higgs boson production and decay using up to 139 fb⁻¹ of proton-proton collision data at $\sqrt{s} = 13$ TeV collected with the ATLAS experiment*, .
- [60] ATLAS collaboration, *Combined effective field theory interpretation of Higgs boson and weak boson production and decay with ATLAS data and electroweak precision observables*, .
- [61] J. de Blas, Y. Du, C. Grojean, J. Gu, V. Miralles, M.E. Peskin et al., *Global SMEFT Fits at Future Colliders*, in *Snowmass 2021*, 6, 2022 [[2206.08326](#)].
- [62] E. Celada, T. Giani, J. ter Hoeve, L. Mantani, J. Rojo, A.N. Rossia et al., *Mapping the SMEFT at high-energy colliders: from LEP and the (HL-)LHC to the FCC-ee*, *JHEP* **09** (2024) 091 [[2404.12809](#)].
- [63] C. Bissolotti, R. Boughezal and K. Simsek, *SMEFT probes in future precision DIS experiments*, *Phys. Rev. D* **108** (2023) 075007 [[2306.05564](#)].
- [64] R. Boughezal, E. Mereghetti and F. Petriello, *Dilepton production in the SMEFT at $O(1/\Lambda^4)$* , *Phys. Rev. D* **104** (2021) 095022 [[2106.05337](#)].
- [65] E. da Silva Almeida, N. Rosa-Agostinho, O.J.P. Éboli and M.C. Gonzalez-Garcia, *Light-quark dipole operators at the LHC*, *Phys. Rev. D* **100** (2019) 013003 [[1905.05187](#)].
- [66] V. Cirigliano, A. Crivellin, W. Dekens, J. de Vries, M. Hoferichter and E. Mereghetti, *CP Violation in Higgs-Gauge Interactions: From Tabletop Experiments to the LHC*, *Phys. Rev. Lett.* **123** (2019) 051801 [[1903.03625](#)].
- [67] J. Kley, T. Theil, E. Venturini and A. Weiler, *Electric dipole moments at one-loop in the dimension-6 SMEFT*, *Eur. Phys. J. C* **82** (2022) 926 [[2109.15085](#)].
- [68] G. Panico, A. Pomarol and M. Riembau, *EFT approach to the electron Electric Dipole Moment at the two-loop level*, *JHEP* **04** (2019) 090 [[1810.09413](#)].
- [69] R.D. Ball et al., *Parton distributions with LHC data*, *Nucl. Phys. B* **867** (2013) 244 [[1207.1303](#)].
- [70] T. Sjostrand, S. Mrenna and P.Z. Skands, *A Brief Introduction to PYTHIA 8.1*, *Comput. Phys. Commun.* **178** (2008) 852 [[0710.3820](#)].
- [71] M. Cacciari, G.P. Salam and G. Soyez, *FastJet User Manual*, *Eur. Phys. J. C* **72** (2012) 1896 [[1111.6097](#)].
- [72] M. Cacciari, G.P. Salam and G. Soyez, *The anti- k_t jet clustering algorithm*, *JHEP* **04** (2008) 063 [[0802.1189](#)].
- [73] E. Conte, B. Fuks and G. Serret, *MadAnalysis 5, A User-Friendly Framework for Collider Phenomenology*, *Comput. Phys. Commun.* **184** (2013) 222 [[1206.1599](#)].
- [74] F. Cascioli, T. Gehrmann, M. Grazzini, S. Kallweit, P. Maierhöfer, A. von Manteuffel et al., *ZZ production at hadron colliders in NNLO QCD*, *Phys. Lett. B* **735** (2014) 311 [[1405.2219](#)].

- [75] L. Chen, J. Davies, G. Heinrich, S.P. Jones, M. Kerner, G. Mishima et al., *ZH production in gluon fusion at NLO in QCD*, *JHEP* **08** (2022) 056 [[2204.05225](#)].
- [76] J.M. Campbell, J.W. Huston and W.J. Stirling, *Hard Interactions of Quarks and Gluons: A Primer for LHC Physics*, *Rept. Prog. Phys.* **70** (2007) 89 [[hep-ph/0611148](#)].
- [77] M.D. Schwartz, *TASI Lectures on Collider Physics*, in *Proceedings, Theoretical Advanced Study Institute in Elementary Particle Physics : Anticipating the Next Discoveries in Particle Physics (TASI 2016): Boulder, CO, USA, June 6-July 1, 2016*, R. Essig and I. Low, eds., pp. 65–100 (2018), DOI [[1709.04533](#)].
- [78] G. Cowan, K. Cranmer, E. Gross and O. Vitells, *Asymptotic formulae for likelihood-based tests of new physics*, *Eur. Phys. J. C* **71** (2011) 1554 [[1007.1727](#)].
- [79] Y. Coadou, *Boosted decision trees*, [2206.09645](#).
- [80] A.S. Cornell, W. Doorsamy, B. Fuks, G. Harmsen and L. Mason, *Boosted decision trees in the era of new physics: a smuon analysis case study*, *JHEP* **04** (2022) 015 [[2109.11815](#)].
- [81] T. Chen and C. Guestrin, *Xgboost: A scalable tree boosting system*, in *Proceedings of the 22nd ACM SIGKDD International Conference on Knowledge Discovery and Data Mining*, KDD '16, ACM, Aug., 2016, DOI.
- [82] F. Pedregosa, G. Varoquaux, A. Gramfort, V. Michel, B. Thirion, O. Grisel et al., *Scikit-learn: Machine learning in Python*, *Journal of Machine Learning Research* **12** (2011) 2825.
- [83] S. Lundberg and S.-I. Lee, *A unified approach to interpreting model predictions*, 2017.